



Molecules with ALMA at Planet-forming Scales (MAPS). XV. Tracing Protoplanetary Disk Structure within 20 au

Arthur D. Bosman¹, Edwin A. Bergin¹, Ryan A. Loomis², Sean M. Andrews³, Merel L. R. van 't Hoff¹, Richard Teague³, Karin I. Öberg³, Viviana V. Guzmán⁴, Catherine Walsh⁵, Yuri Aikawa⁶, Felipe Alarcón¹, Jaehan Bae^{7,24}, Jennifer B. Bergner^{8,24}, Alice S. Booth^{5,9}, Gianni Cataldi^{6,10}, L. Ilseore Cleeves¹¹, Ian Czekala^{12,13,14,15,16,24}, Jane Huang^{1,3,24}, John D. Ilee⁵, Charles J. Law³, Romane Le Gal^{3,17,18,19}, Yao Liu²⁰, Feng Long³, François Ménard¹⁷, Hideko Nomura¹⁰, Laura M. Pérez²¹, Chunhua Qi³, Kamber R. Schwarz^{22,24}, Anibal Sierra²¹, Takashi Tsukagoshi¹⁰, Yoshihide Yamato⁶, David J. Wilner³, and Ke Zhang^{23,25}

¹ Department of Astronomy, University of Michigan, 323 West Hall, 1085 S. University Ave., Ann Arbor, MI 48109, USA; arbos@umich.edu

² National Radio Astronomy Observatory, Charlottesville, VA 22903, USA

³ Center for Astrophysics | Harvard & Smithsonian, 60 Garden St., Cambridge, MA 02138, USA

⁴ Instituto de Astrofísica, Pontificia Universidad Católica de Chile, Av. Vicuña Mackenna 4860, 7820436 Macul, Santiago, Chile

⁵ School of Physics and Astronomy, University of Leeds, Leeds LS2 9JT, UK

⁶ Department of Astronomy, Graduate School of Science, The University of Tokyo, Tokyo 113-0033, Japan

⁷ Earth and Planets Laboratory, Carnegie Institution for Science, 5241 Broad Branch Road NW, Washington, DC 20015, USA

⁸ University of Chicago Department of the Geophysical Sciences, Chicago, IL 60637, USA

⁹ Leiden Observatory, Leiden University, 2300 RA Leiden, The Netherlands

¹⁰ National Astronomical Observatory of Japan, 2-21-1 Osawa, Mitaka, Tokyo 181-8588, Japan

¹¹ University of Virginia, 530 McCormick Rd., Charlottesville, VA 22904, USA

¹² Department of Astronomy and Astrophysics, 525 Davey Laboratory, The Pennsylvania State University, University Park, PA 16802, USA

¹³ Center for Exoplanets and Habitable Worlds, 525 Davey Laboratory, The Pennsylvania State University, University Park, PA 16802, USA

¹⁴ Center for Astrostatistics, 525 Davey Laboratory, The Pennsylvania State University, University Park, PA 16802, USA

¹⁵ Institute for Computational & Data Sciences, The Pennsylvania State University, University Park, PA 16802, USA

¹⁶ Department of Astronomy, 501 Campbell Hall, University of California, Berkeley, CA 94720-3411, USA

¹⁷ Univ. Grenoble Alpes, CNRS, IPAG, F-38000 Grenoble, France

¹⁸ IRAP, Université de Toulouse, CNRS, CNES, UT3, 31400 Toulouse, France

¹⁹ IRAM, 300 rue de la piscine, F-38406 Saint-Martin d'Hères, France

²⁰ Purple Mountain Observatory & Key Laboratory for Radio Astronomy, Chinese Academy of Sciences, Nanjing 210023, People's Republic of China

²¹ Departamento de Astronomía, Universidad de Chile, Camino El Observatorio 1515, Las Condes, Santiago, Chile

²² Lunar and Planetary Laboratory, University of Arizona, 1629 E. University Blvd., Tucson, AZ 85721, USA

²³ Department of Astronomy, University of Wisconsin–Madison, 475 N. Charter St., Madison, WI 53706, USA

Received 2021 February 15; revised 2021 June 2; accepted 2021 June 6; published 2021 November 3

Abstract

Constraining the distribution of gas and dust in the inner 20 au of protoplanetary disks is difficult. At the same time, this region is thought to be responsible for most planet formation, especially around the water ice line at 3–10 au. Under the assumption that the gas is in a Keplerian disk, we use the exquisite sensitivity of the Molecules with ALMA at Planet-forming Scales (MAPS) ALMA large program to construct radial surface brightness profiles with a ~ 3 au effective resolution for the CO isotopologue $J=2-1$ lines using the line velocity profile. IM Lup reveals a central depression in ^{13}CO and C^{18}O that is ascribed to a pileup of $\sim 500 M_{\oplus}$ of dust in the inner 20 au, leading to a gas-to-dust ratio of around <10 . This pileup is consistent with an efficient drift of grains ($\gtrsim 100 M_{\oplus} \text{ Myr}^{-1}$) and a local gas-to-dust ratio that suggests that the streaming instability could be active. The CO isotopologue emission in the GM Aur disk is consistent with a small (~ 15 au), strongly depleted gas cavity within the ~ 40 au dust cavity. The radial surface brightness profiles for both the AS 209 and HD 163296 disks show a local minimum and maximum in the C^{18}O emission at the location of a known dust ring (~ 14 au) and gap (~ 10 au), respectively. This indicates that the dust ring has a low gas-to-dust ratio (>10) and that the dust gap is gas-rich enough to have optically thick C^{18}O . This paper is part of the MAPS special issue of the Astrophysical Journal Supplement.

Unified Astronomy Thesaurus concepts: Millimeter astronomy (1061); Protoplanetary disks (1300); Planet formation (1241)

1. Introduction

Exoplanet statistical studies imply that the majority of solar-type stars have a planet within 1 au of the star, with observed close-in planets spanning a wide mass range, from sub-Earth-to multi-Jupiter-mass planets (e.g., Johnson et al. 2010; Mulders 2018). It is hypothesized that a large portion of these planets form relatively close to the star, with the water ice line posited as a favored location to facilitate planet formation (e.g.,

Ciesla & Cuzzi 2006; Lyra et al. 2010; Cridland et al. 2019; Fernandes et al. 2019). This primary zone of planet formation is difficult to probe, as the physical scales are small, <10 au in radius, corresponding to angular sizes of $<0''.1$ in the closest star-forming regions (140–200 pc).

The inner 20 au is also critical in terms of disk physics. It is the region where the magnetorotational instability is thought to be strongly suppressed and accretion toward the star is assumed to be powered by magnetohydrodynamic winds (Armitage 2011). Internal photoevaporative winds are also thought to be launched from the inner 20 au as well (for a review, see Ercolano & Pascucci 2017). Changes in transport speed of the gas, as well as

²⁴ NASA Hubble Fellowship Program Sagan Fellow.

²⁵ NASA Hubble Fellow.

the launching of a wind, are thought to have profound effects on the structure of the gas disk, which then impacts the dust disk as well. Observing structure in the inner 20 au could thus reveal information on a host of processes.

Studies of this primary planet-forming zone have focused on either the composition of the molecular gas within the water ice line or the structure of the gas and dust disk near the dust sublimation radius. Compositional studies of the disk inside the water ice line are driven by near- and mid-infrared observations with, for example, VLT-CRIRES, Keck-NIRSPEC, VLT-VISIR, and Spitzer-IRS. The observations generally lack the resolution to spatially resolve the inner disk, but it is only the inner disk that has the physical conditions necessary to produce emission of the 2–35 μm rotational and rovibrational lines that these instruments target (e.g., Carr & Najita 2008; Pontoppidan et al. 2010; Salyk et al. 2011). These observations have taught us that the surface layers of the inner disk are hot (500–1000 K; e.g., Salyk et al. 2011), dust poor (e.g., Meijerink et al. 2009), and strongly UV irradiated (Pontoppidan & Blevins 2014; Bosman et al. 2018).

Directly imaging structure in the inner tens of astronomical units is difficult, as high-resolution optical and infrared imagers either obscure this region behind a coronagraph or have the stellar point-spread function overwhelm the disk emission (e.g., Avenhaus et al. 2017). Submillimeter interferometry can now reach 30 mas (~ 5 au) resolution in the dust, barely resolving this region (e.g., ALMA Partnership et al. 2015; Andrews et al. 2018). However, gas emission-line studies in protoplanetary disks are generally limited to 100 mas in light of sensitivity and integration time considerations (e.g., Öberg et al. 2021). Infrared interferometry can reach a resolution down to 1 mas in both the gas and dust, which would easily resolve the planet formation regions; however, these instruments generally are not able to probe scales larger than ~ 5 au and are most sensitive to emission on scales smaller than 1 au (Dullemond & Monnier 2010; Menu et al. 2015; Gravity Collaboration et al. 2017; Lazareff et al. 2017). There is thus a gap in our knowledge of gas structure at few au scales in the inner ~ 20 au from imaging studies.

Exploiting the spatial information in high resolving power spectra ($\frac{\lambda}{\Delta\lambda} = R > 25,000$), it is possible to close this gap in our knowledge for gas emission lines. This has mostly been applied to the strong infrared CO rovibrational lines around 4.7 μm (e.g., Pontoppidan et al. 2008; van der Plas et al. 2015; Banzatti & Pontoppidan 2015; Bosman et al. 2019). In particular, these observations have been used to map the CO column density profile in the dust cavity of transition disk HD 139614 (Carmona et al. 2017).

The high resolving power of submillimeter interferometers ($R > 10^6$) also allows the use of kinematic information to extract spatial information. Notable results include the inference of significant molecular gas within the millimeter dust hole in TW Hya at radii < 4 au (Rosenfeld et al. 2012), a gap in the molecular gas in GM Aur (Dutrey et al. 2008) that has just recently been resolved (Huang et al. 2020; Law et al. 2021). It has further been used to constrain the gas distribution in debris disks (Hales et al. 2019) and the CO gas mass within an unresolved CO snowline in a handful of Class I and II sources (Zhang et al. 2020a, 2020b).

In this paper, we use the high sensitivity and spectral resolving power of the Molecules with ALMA at Planet-forming Scales (MAPS)²⁶ data (Czekala et al. 2021; Law et al. 2021;

Öberg et al. 2021) to zoom in on the CO emission in the inner few astronomical units of the targeted disks (AS 209, IM Lup, GM Aur, HD 163296, and MWC 480). Law et al. (2021) presents central flux depressions in the CO line emission in four out of five (all except MWC 480) of the MAPS sources in some or all of the isotopologue lines. The goals of this paper are to look for and, where possible, characterize and explain unresolved structure in the CO emission. We are thus tracing gas structure down to the primary planet-forming zone.

2. Observations

This study uses CO line data taken as part of the MAPS ALMA Large Program (2018.1.01055.L), specifically the ^{12}CO , ^{13}CO and, C^{18}O $J = 2-1$ and the ^{13}CO and C^{18}O $J = 1-0$ isotopologue lines.

The reduction and imaging procedure of these data is outlined in Öberg et al. (2021) and Czekala et al. (2021). From the standard data products we used the circularized, $0''.3$ beam images for all isotopologue lines. For the $J = 2-1$ lines, we also use images with minor differences in the imaging procedure, namely, velocity range imaged for these lines is $4\times$ as large as detailed in Czekala et al. (2021) to get a proper baseline of line-free channels (See Table 1 for the velocity ranges). With this velocity range, image cubes with a $0''.15$ and $0''.3$ circularized beam are created for all three isotopologues. Furthermore, we use line+continuum CLEAN masks, which combine the Keplerian mask with an elliptical mask that encompasses the millimeter disk, even though we are imaging the continuum-subtracted visibilities. The line+continuum CLEAN masks make sure that all on-source flux in the high-velocity channels is included. Unless otherwise noted, we use these wider CO images for our analysis.

For these wider velocity range images, as for the fiducial CO images (^{13}CO and C^{18}O , $J = 1-0$; ^{12}CO , ^{13}CO , and C^{18}O , $J = 2-1$), spectra are extracted from the image cubes by summing the pixels either in a circular aperture or in the CLEAN mask.

3. Methods

Figure 1 shows the spectral line profiles extracted for the ^{12}CO $J = 2-1$ line toward all five of the MAPS sources using a series of circular apertures with a radius, ranging between $0''.2$ and $0''.8$. The smallest aperture ($0''.2$) has the advantage that it includes the fewest pixels, and that at large velocities (and thus small emitting radii) it is the most precise measurement. Comparison to larger apertures shows that around the velocities corresponding to 10–20 au (around $0''.15$) the spectrum from the smallest aperture starts to deviate, as it no longer encompasses all the flux in the image.

The symmetry of the line profiles has been studied in Appendix A.1, where we only find nonsymmetric emission in AS 209 and HD 163296, which will be masked in the rest of the analysis (see Figure 1). A comparison of the $J = 2-1$ and $J = 1-0$ line profiles is presented in Appendix A.2. No clear evidence of the lower-frequency line probing deeper into the disk, or significantly less impact of the continuum subtraction, is seen in the comparison of the line profiles.

The spectrum used for the radial profile fitting is a combination of the spectra extracted with the different apertures. The spectra are extracted from the wide velocity range $J = 2-1$ isotopologue

²⁶ <http://www.alma-maps.info>

Table 1
Source Properties

Source	M_* (M_\odot)	Incl. (deg)	v_{sys} (km s ⁻¹)	v_{range} (km s ⁻¹)	Reference
IM Lup	1.1	47.5	4.5	−19.5, 28.5	(Pinte et al. 2018; Huang et al. 2018; Czekala et al. 2021)
GM Aur	1.1	53.2	5.6	−22.4, 33.6	(Macías et al. 2018; Huang et al. 2020)
AS 209	1.2	35.0	4.6	−29.4, 38.6	(Huang et al. 2017, 2018; Czekala et al. 2021)
HD 163296	2.0	46.7	5.8	−33.0, 44.8	(Andrews et al. 2018; Huang et al. 2018; Teague et al. 2019)
MWC 480	2.1	37.0	5.1	−26.9, 37.1 ^a	(Piétu et al. 2007; Simon et al. 2019; Liu et al. 2019)

Note.^a Available velocity range for ¹³CO and C¹⁸O is only −6.9 and 17.1 km s⁻¹, respectively.

images. For channels that have emission that should only originate within 0''.05, a 0''.4 aperture is used, and for emission originating between 0''.05 and 0''.25, a 0''.6 aperture is used. For these images a baseline 0''.15 circularized beam is used. For emission originating between 0''.25 and 0''.5, the spectrum is extracted with a 0.8'' aperture from the images that have a 0''.3 circularized beam. As 0''.5 translates to 50–80 au, this spectrum contains all the flux necessary for our purposes. This has been checked against the flux extracted from within the CLEAN mask. For any of our further analysis, we will not consider emission from radii >40 au. The velocity range in the spectra that corresponds to these radii is never taken into account in the fitting.

Flux errors are estimated by taking the rms of the complete ALMA data cube outside the CLEAN mask and multiplying that by the square root of the number of beams that fit within the spectral extraction aperture.

The reconstruction of the radial intensity profiles ($I(R)$) is based on the assumption that all the disk emission is coming from gas in Keplerian rotation. For gas in Keplerian rotation, the maximal projected velocity that is achieved at a given radius is given by

$$v_{\text{max}}(R) = \sqrt{\frac{GM_*}{R}} \sin(i), \quad (1)$$

where G is Newton’s gravitational constant, M_* the stellar mass, R the radius, and i the inclination of the disk. Stellar mass and inclinations used in this paper are listed in Table. 1. This implies that emission at velocity offsets larger than a given value must be generated within the radius as given by Equation (1). For each of the disks these relations are given in Figure 12. This implies a relation between $\frac{dF(v)}{dv}$ and $I(R)$. While it is in principle possible to use this relation directly to derive $I(R)$ from the extracted spectra, we do not do this, but will instead use a very simple forward model to fit the spectra ($F(v)$) with a radial intensity profile. Fitting a forward model makes it easier to directly account for the finite velocity resolution and estimate the effect of noise in the spectra on the inferred brightness profiles. Full details of the fitting procedure are given in Appendix B.

4. Radial Intensity Profiles

Figure 2 shows the radial surface brightness profiles extracted from the CO isotopologue line profiles for the five MAPS sources. These surface brightness profiles show features on scales that are not distinguishable in the CLEANED images with 0''.15 resolution.

The surface brightnesses of the ¹³CO and C¹⁸O isotopologues are low in the inner regions of the IM Lup disk. The C¹⁸O surface brightness is below our detection threshold within 30 au, and the ¹³CO surface brightness drops below the detection threshold around 20 au. The ¹²CO surface brightness profiles show some structure between 5 and 15 au, with a local minimum that is a factor of two lower than the surrounding surface brightness at ~8 au. Given the large errors at these radii, it is assumed that these are driven by the noise in the data.

The radial profiles of the GM Aur disk all show a strong drop in emission in the inner region. ¹²CO drops inside 15 au, while ¹³CO and C¹⁸O drop inside of 20 au. This leads to very similar C¹⁸O and ¹³CO profiles, with the ¹³CO profile being slightly brighter. Comparing to the radial profiles derived from the CLEANED images by Law et al. (2021) (see Appendix C), the surface brightness derived from the line profiles shows a steeper drop in all isotopologues.

The radial surface brightness profiles of the AS 209 disk are rich in substructures. The ¹²CO profile appears centrally peaked and has a local minimum at ~3 au followed by a local maximum at ~8 au with a monotonically decreasing flux toward larger radii. The ¹³CO seems to follow the ¹²CO radial profile relatively well, showing the same peak at 8 au and dropping inward from this radius, after which the emission becomes indistinguishable from the noise. The C¹⁸O shows a strong decrease in surface brightness inward of 20 au that is not seen in the ¹²CO and ¹³CO lines. At low significance, the C¹⁸O also shows a maximum at 8 au, together with the other isotopologues.

The surface brightness profiles of the HD 163296 disk only probe down to 5 au, as the velocity channels corresponding to smaller radii are contaminated on both the blue- and redshifted side. The ¹²CO and ¹³CO surface brightness profiles show low-amplitude (less than a factor 2) variations over the entire 5–30 au range. These amplitude variations do not seem to be consistent between the lines, however. The C¹⁸O shows strong (more than a factor 2) oscillations between 7 and 15 au. At around 9 au there is a peak in the surface brightness distribution, leading to comparable C¹⁸O and ¹³CO fluxes. Within 9 au there is a sharp drop in surface brightness to below our detection threshold. Outside of 9 au the flux drops to a local minimum at 12 au.

The radial surface brightness profiles of ¹²CO and ¹³CO around MWC 480 show similar low-amplitude deviations to HD 163296, with ¹³CO additionally showing a strong peak around 10 au. The C¹⁸O surface brightness profile shows a strong dip at the same location. The ¹²CO peaks strongly toward the inner disk.

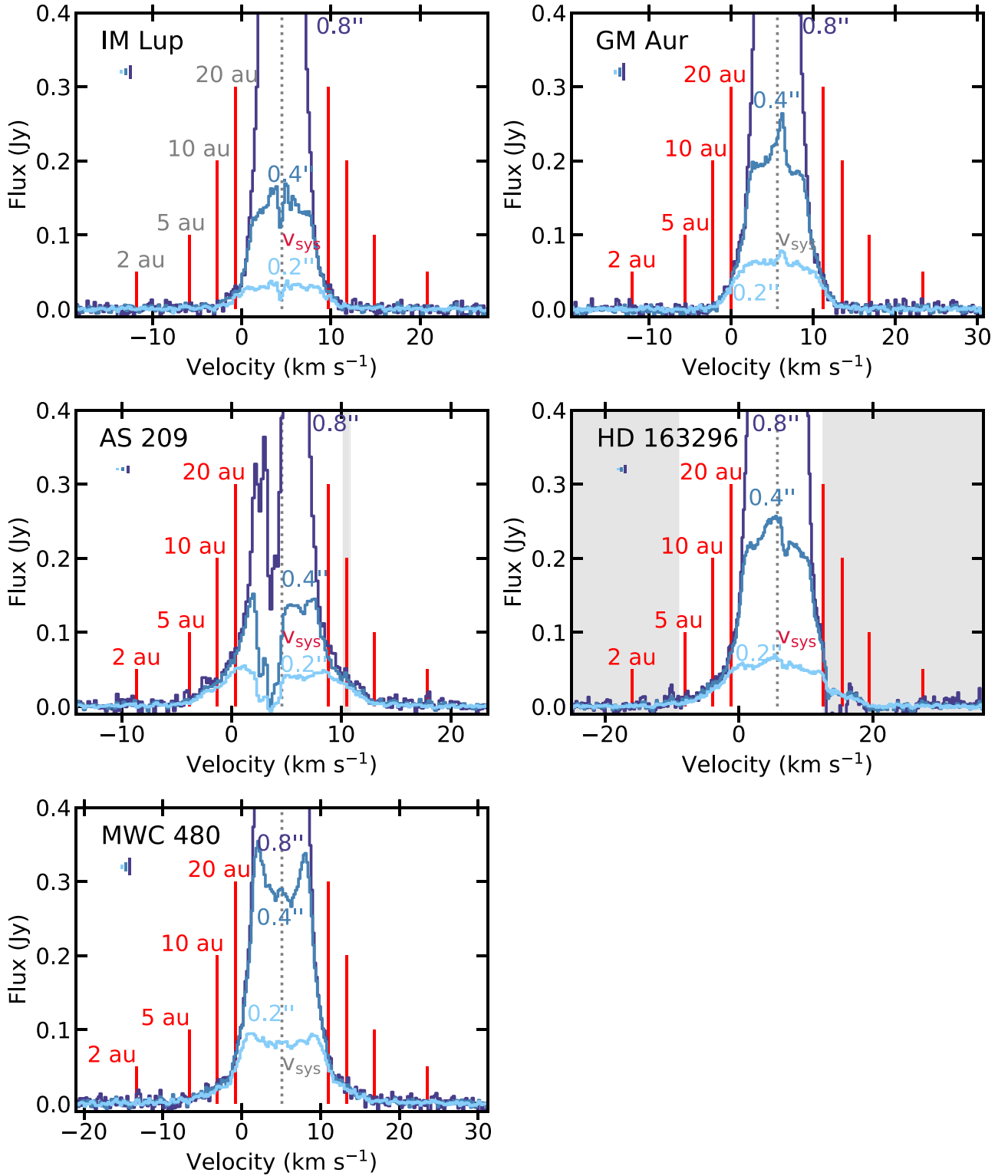


Figure 1. CO $J = 2-1$ spectrum of all our sources as extracted with different circular apertures. The apertures have a radius between $0''.2$ and $0''.8$. The vertical bars under the disk names show the error bars for the extracted spectra. The gray dotted vertical line shows the systemic velocity; red vertical lines show the velocity that corresponds to the maximal projected velocity for 2, 5, 10, and 20 au; and the gray shaded areas show the regions that have been masked in the radial profile determination (these regions are discussed in Appendix A.1).

5. The Effect of Dust on Line Emission

The inner regions of these five protoplanetary disks show a large variety of structures that are not well traced by imaging with the high ($0''.15$) resolution of the MAPS data. Four of the disks, AS 209, IM Lup, HD 163296, and MWC 480, have

strong dust emission in the inner 30 au. AS 209 and HD 163296 also have previously resolved structure in the dust disk in this region (Andrews et al. 2018; Huang et al. 2018). Before interpreting these structures, it is necessary to discuss the effects of dust on the line emission.

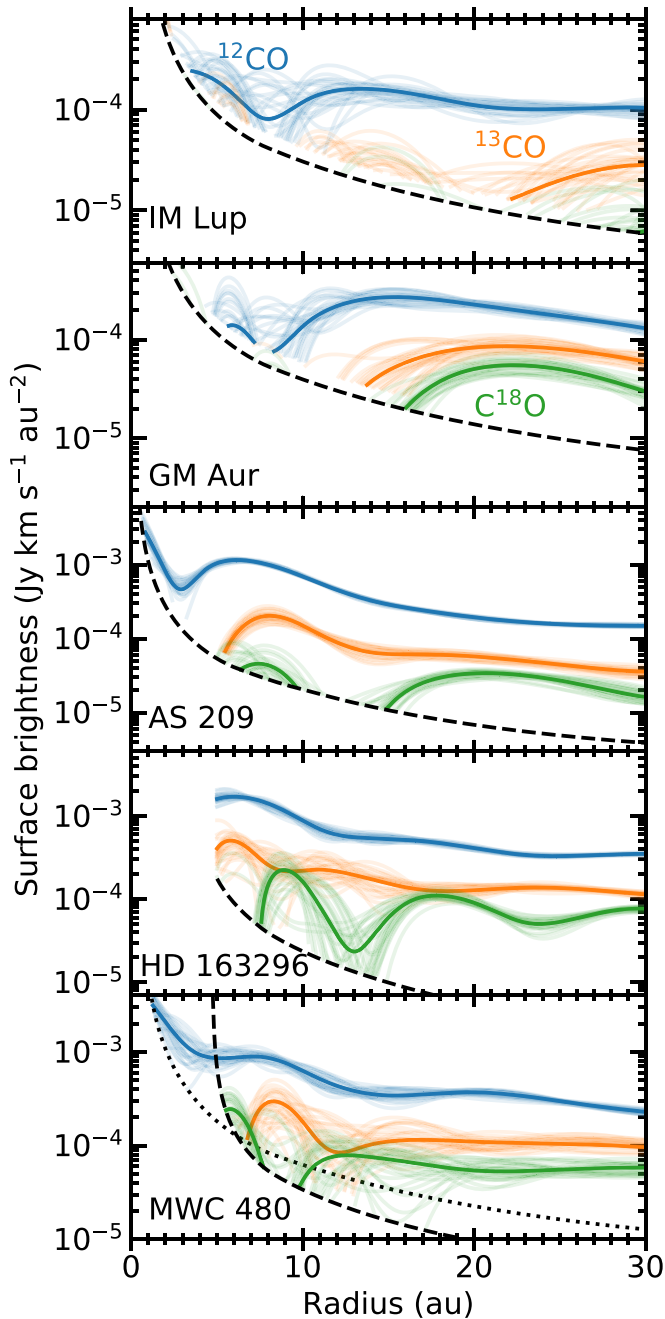


Figure 2. Radial profiles of the five MAPS sources as constrained from the ^{12}CO (blue), ^{13}CO (orange), and C^{18}O (green) $J = 2-1$ spectra. The fit to the data is shown with a thick line. Thin lines show 30 fits of the data after flux offsets had been applied to each velocity bin according to the observational uncertainties. These lines give an estimate on the uncertainty in the strength, depth, and location of the features. The black dashed line shows the lower limit to the flux that can be measured at each radius for the C^{18}O spectra. When a radial surface brightness profile drops below its detection limit, it is not plotted. Due to slightly different rms values for the ^{12}CO , ^{13}CO , and C^{18}O data cubes, this does not happen exactly at the dashed line for the ^{12}CO and ^{13}CO radial profiles. The inner radius for HD 163296 is ~ 5 au, as the highest velocities had to be masked out. For MWC 480 a wider velocity range was available for the ^{12}CO than the ^{13}CO and C^{18}O ; in this case the ^{12}CO sensitivity is given with a black dotted line.

Given the limited velocity coverage of the CO spectral windows ($100\text{--}200\text{ km s}^{-1}$), which is on par with the infrared, rovibrational CO line widths (e.g., Brown et al. 2013; Banzatti et al. 2017), a single spectral window cannot be used to conclusively distinguish high-velocity (small radii) CO emission

from continuum emission. All the spectra used here are thus continuum subtracted, using the dust emission information in all spectral windows combined for an accurate continuum determination.

The role of the dust optical depth on the CO emission profiles is not lessened in this way, and standard checks, such as comparing with continuum or line+continuum images, are not possible. It is thus worth discussing the effects of (unresolved) continuum emission on the line radial profiles. As the dust emission of all the MAPS disks has been modeled (Sierra et al. 2021; Zhang et al. 2021), there is a good estimate of the average millimeter dust optical depth in the inner few tens of au. The millimeter emission of GM Aur drops within 40 au, with multiband observations implying that this emission is optically thin. AS 209 and HD 163296 appear to be optically thin around 220 GHz in dust emission down to 20 au assuming a nonscattering dust model (Sierra et al. 2021; Zhang et al. 2021); however, the dust model including scattering and the evidence of dust substructure within 20 au imply that dust is optically thick in some regions within 40 au (Andrews et al. 2018; Huang et al. 2018; Guzmán et al. 2018; Sierra et al. 2021). IM Lup and MWC 480 are consistent with fully optically thick emission within ~ 40 au even without assuming strong scattering at millimeter wavelengths (Liu et al. 2019; Sierra et al. 2021; Zhang et al. 2021).

Optically thick dust has several effects on the observed line emission. Aside from obscuring gas under the millimeter dust photosphere, it also produces a background flux for the line emission originating above the dust emission surface. When gas and dust temperatures differ, there will still be a line visible, either in emission or in absorption, and gas properties can still be extracted (see, e.g., Weaver et al. 2018). There is a relevant edge case, however, when gas temperature (or excitation temperature) and dust temperature are the same over the line of sight. This can happen in a vertically isothermal layer in the inner disk.

The surface brightness profiles of the IM Lup, AS 209, HD 163296, and MWC 480 disks show drops of factors of 3 or more. It is necessary to consider these surface brightness declines as the result of optically thick dust in an isothermal layer and investigate the exact conditions necessary to cause these strong surface brightness drops.

5.1. Line Emission with Dust Scattering

To investigate this, we consider two very simplified physical configurations as shown in Figure 3. We consider an isothermal layer of temperature $T_{\text{iso}} = T_{\text{ex}} = T_{\text{dust}}$ that has the line- and dust-emitting region either completely overlapping or vertically completely separated. For each of these configurations we derive an expression for the continuum-subtracted line flux and discuss the conditions under which the continuum-subtracted line emission is most efficiently diminished.

When looking at millimeter wavelengths, scattering by dust is not negligible. The scattering opacity at a wavelength of 1 mm from grains with a size distribution $n(a) \propto a^p$, with $p = -3.5$, between $0.005\text{ }\mu\text{m}$ and 1 mm is a factor of 10 more than the absorption opacity (Birnstiel et al. 2018; Zhang et al. 2021). This reduces the continuum flux up to a factor of 4 (see Zhu et al. 2019, for a full discussion). Following Zhu et al. (2019), we write the optically thick dust intensity as $I_{\text{dust}} = \chi B_{\nu}(T_{\text{iso}})$; χ is the intensity reduction coefficient and

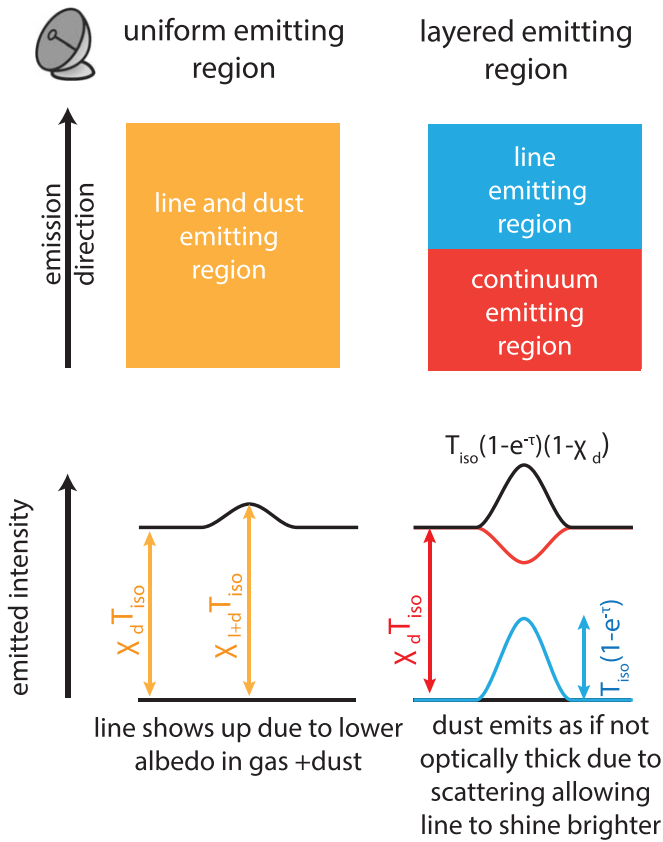


Figure 3. Schematic representation of the expected line strengths from an isothermal layer that has an optically thick dust layer and an optically thin gas contribution. The scenario in orange (left, Equation (4)) shows an emission layer where gas and dust are well mixed. The scenario on the right (Equation (5)) depicts a molecular line-emitting region (blue) on top of a dust (continuum) emitting region (red). In all cases the observer is assumed to look upon the layers from above as noted by the telescope dish. In the bottom panels the expected emission of this layer around a gas spectral line is shown; the observed spectrum is shown in black in the right panel, and the continuum and gas contribution to the spectrum is shown in red and blue, respectively. χ_d refers to the dust intensity reduction coefficient (Equation (2), Zhu et al. 2019), and χ_{l+d} refers to the line and dust intensity reduction coefficient (Equation (3)).

is approximately given as (see Zhu et al. 2019, Equation (13))

$$\chi \approx \sqrt{1 - \omega} = \sqrt{1 - \kappa_{\text{scat}} / (\kappa_{\text{abs}} + \kappa_{\text{scat}})}, \quad (2)$$

where κ_{scat} and κ_{abs} are the scattering and absorption opacity, respectively, and ω is the dust albedo. If line and dust are emitting from the same medium, the line + continuum intensity reduction coefficient has to be used. This is given by

$$\chi_{\text{line+dust}} \approx \sqrt{1 - \frac{\kappa_{\text{scat, dust}}}{(\kappa_{\text{abs, dust}} + \kappa_{\text{abs, line}} + \kappa_{\text{scat, dust}})}}. \quad (3)$$

Note that the absorption of photons by molecules does not have a scattering component associated with it, as such $\chi_{\text{line+dust}} > \chi_{\text{dust}}$ always holds. Assuming that the dust optical depth $\tau_{\text{dust}} \gg 1$, the continuum-subtracted line intensity I_{L-C} is given by

$$I_{L-C} = \chi_{\text{line+dust}} B_{\nu}(T_{\text{iso}}) - \chi_{\text{dust}} B_{\nu}(T_{\text{dust}}) = B_{\nu}(T_{\text{iso}})(\chi_{\text{line+dust}} - \chi_{\text{dust}}), \quad (4)$$

with $B_{\nu}(T)$ the blackbody radiation. In this case (Figure 3, left), the continuum-subtracted line emission only disappears if the opacity of the line is negligible compared to the dust opacity, as that would result in $\chi_{\text{line+dust}} \approx \chi_{\text{dust}}$ (see Section 5.2, for the necessary conditions for CO).

In a protoplanetary disk, the line emission is generated over a larger vertical extent than the millimeter continuum owing to the larger millimeter-sized dust grains being settled toward the midplane (e.g., Dutrey et al. 2017; Zhang et al. 2017). Equation (4) can be modified to assume that the line- and continuum-generating layers are separated, with the line-generating layer closer to the observer (Figure 3, right). This could be the case for disk surface gas that is lofted by hydrostatic equilibrium to greater heights than the settled dust-rich midplane. When considering the effects of scattering, the line emission will appear to be stronger than in the fully mixed case. In this two-layer case, using $\chi_{\text{line}}=1$, and again using $\tau_{\text{dust}} \gg 1$, we can write

$$\begin{aligned} I_{L-C} &= \chi_{\text{line}} B_{\nu}(T_{\text{ex}})(1 - e^{-\tau_{\text{line}}}) \\ &+ \chi_{\text{dust}} B_{\nu}(T_{\text{dust}}) e^{-\tau_{\text{line}}} \\ &- \chi_{\text{dust}} B_{\nu}(T_{\text{dust}}) \\ &= B_{\nu}(T_{\text{iso}})(1 - e^{-\tau_{\text{line}}}) \\ &- \chi_{\text{dust}} B_{\nu}(T_{\text{dust}})(1 - e^{-\tau_{\text{line}}}) \\ &= B_{\nu}(T_{\text{iso}})(1 - e^{-\tau_{\text{line}}})(1 - \chi_{\text{dust}}). \end{aligned} \quad (5)$$

In this case, there thus will always be line emission visible above an optically thick dust continuum unless the dust does not scatter its own radiation, that is, $\chi_{\text{dust}} \approx 1$ (which reduces to the case discussed in Rosotti et al. 2021).

5.2. Fully Suppressing Line Emission with Optically Thick Dust

What is left to understand is under which physical conditions it is possible to suppress the line flux significantly. In both Equations (4) and (5) the line flux drops significantly when χ_{dust} approaches 1, which implies negligible scattering. For particles of astronomically relevant composition and assuming $p = -3.5$, this happens when the maximum grain size is smaller than 0.1 mm, or larger than 10 cm (Zhu et al. 2019). Grains of these sizes, however, have at least an order of magnitude lower total (absorption+scattering) opacity compared to millimeter-sized grains, implying that $10\times$ more mass is needed to make the midplane optically thick at 1–3 mm wavelengths (Sierra et al. 2021). This would imply large pileups of dust in the regions that are optically thick.

Line flux could also be significantly reduced if the line-emitting layer and continuum-emitting layer are mixed. Here dust scattering and absorption modify the line flux. This would entail the lofting of millimeter-sized grains to the layer from which the molecule of interest is emitting. In this case, dust scattering and absorption dominate the total opacity, even at line center. Taking the CO $J=2-1$ line as an example, we can estimate the local gas-to-dust ratios necessary. For simplicity a temperature of 50 K, a CO line width of 1 km s^{-1} , and an abundance with respect to H_2 of 10^{-4} are assumed. Under these conditions, CO gas has a gas mass opacity of $\sim 1000 \text{ cm}^2 \text{ g}^{-1}$ (Schöier et al. 2005; Endres et al. 2016), compared to the $0.3 \text{ cm}^2 \text{ g}^{-1}$ for millimeter-sized dust at a gas-to-dust ratio of 100 (Birnstiel et al. 2018). $^{12}\text{CO } J=2-1$ should thus only be affected by dust opacity when the gas-to-dust ratio drops to values around 0.03, which is unlikely. However, for ^{13}CO and

C^{18}O , which are 69 and 550 times less abundant (Wilson & Rood 1994), gas-to-dust ratios of ~ 2 and ~ 15 can cause significant suppression of the line flux. This assumes that the CO abundance is 10^{-4} ; for lower CO abundances, less dust would be necessary.

6. Discussion

6.1. Evidence for Pebble Drift Feeding the Inner IM Lup Disk

IM Lup shows a strong surface brightness drop in ^{13}CO and C^{18}O in the inner ~ 30 au in the image-derived radial profiles and in surface brightness profiles derived via the line profiles. Dust models suggest that the dust continuum emission is optically thick in the inner regions (Cleeves et al. 2017; Sierra et al. 2021), with optical depths >3 within 40 au (Sierra et al. 2021). As argued in Section 5.2, for this dust to significantly affect the C^{18}O emission, the gas-to-dust ratio must be lower than 100. In the case in which the dust is nonscattering, at least $500 M_{\oplus}$ is necessary to make the dust optically thick and thus suppress the line emission within the inner 20 au. The amount of dust necessary if the grains are around millimeter sized and vertically extended is not straightforward to estimate owing to the complex interaction between line emission and the scattering of the dust. As calculated in Section 5.2, $500 M_{\oplus}$, which implies a gas-to-dust ratio of ~ 10 , is of the right magnitude to impact the line emission.

To better constrain the mass necessary to reproduce the observations in the case of a vertically extended grain population, we calculated the CO line emission in a couple of Dust And Lines (DALI) models (Bruderer et al. 2012; Bruderer 2013). These toy models are tuned to roughly match the CO column derived at ~ 100 au radii by Zhang et al. (2021), assuming a CO abundance of 10^{-5} (model setup is presented in Appendix D). This model is just a representative model to see the effects of dust and is not finely tuned to the IM Lup (inner) disk. The distribution and amount of large dust within 20 au are varied in these models. In the fiducial model, the large dust (up to 1 mm) is settled; in all other models, this large dust population is well mixed in with the gas. At the same time, the amount of large dust is increased by a factor of 1, 10, and 100, exploring gas-to-dust ratios of 100, 10, and 1. The radial profiles derived from model line profiles, and the IM Lup observations as a comparison are shown in Figure 4. The goal of these models is not to fit the data perfectly but to see the effects of different dust distributions on the CO isotopologue emission.

The model ^{12}CO surface brightness drops uniformly when the amount of dust in the atmosphere is increased. This is caused by the extra dust in the atmosphere lowering the gas and dust temperature, due to decreased penetration of optical and UV photons. The ^{13}CO and C^{18}O emission in the models is also impacted by the additional large dust. Outside of 20 au, a brightness drop like that for ^{12}CO is seen. Inward of 20 au there is an extra drop in models with 10 and 100 times more dust. This allows us to reproduce the order-of-magnitude drop in C^{18}O and ^{13}CO intensities.

The amount of dust necessary to obscure the line photons in the model is between 400 and 4000 M_{\oplus} within 20 au. This is in agreement with the amount of dust derived from multi-wavelength continuum fitting, which finds $\sim 500 M_{\oplus}$ of grains within 20 au (Sierra et al. 2021). The minimal mass necessary

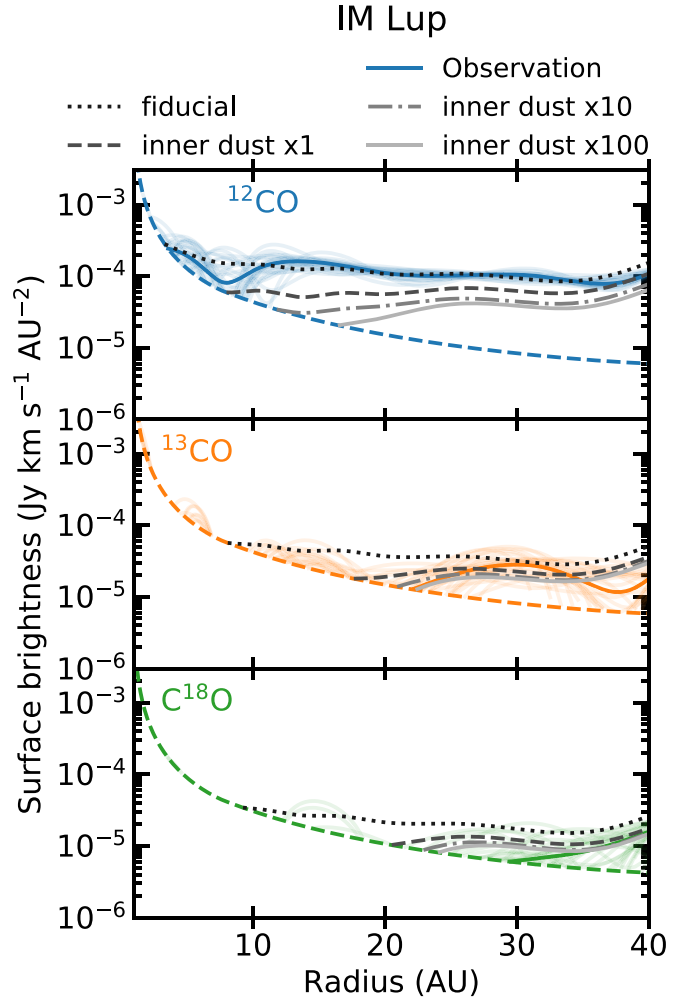


Figure 4. CO radial profiles of IM Lup compared with model radial profiles of ^{12}CO (top), ^{13}CO (middle), and C^{18}O (bottom), for which the large dust vertical distribution is varied within 20 au. Colored solid lines show the CO isotopologue radial surface brightness profiles, and the dashed lines show the detection limit (see Figure 2). Models are shown in gray scale in different line styles. Apart from the fiducial model, all models have the large dust fully vertically mixed with the gas, and the models shown with dashed-dotted and solid lines have the large dust within 20 au enhanced by a factor of 10 and 100, respectively. Surface densities and model description are given in Appendix D.

to explain the CO observations is thus $\sim 500 M_{\oplus}$ regardless of grain size. However, if the grains have a significant scattering opacity, they will need to be vertically well mixed. Grains of 1 mm have a Stokes number of $\text{St} = 4 \times 10^{-3}$ at 20 au ($\Sigma_{\text{gas}} \approx 100$). To efficiently mix these into the surface layers, we need a turbulent $\alpha > \text{St} = 4 \times 10^{-3}$ (Dubrulle et al. 1995). This is significantly higher than the turbulence expected for an inner-disk dead zone (e.g., Gammie 1996).

The masses for the millimeter grain models assume that the CO abundance in the inner 20 au is 10^{-5} . If it were increased to 10^{-4} , this would imply 10 times more large dust, as well as a gas-to-dust ratio of 0.1–1. The model thus needs more dust than the minimum amounts estimated from the analytical derivation (Section 5.2).

Given the young ~ 1 Myr age of IM Lup (Mawet et al. 2012), it seems reasonable that the large agglomeration of dust in the inner disk is due to radial drift of the grains. Radial drift can explain both the strong agglomeration of dust within the 1 Myr timescale and the specific transport of dust, but not

gas, leading to low gas-to-dust ratios. Radial dust transport rates of $\gtrsim 100 M_{\oplus} \text{Myr}^{-1}$ are often invoked to quickly build the cores of gas giants in pebble accretion models (e.g., Bitsch et al. 2019), which appears possible in the IM Lup disk.

The low gas-to-dust ratios derived in the inner disk would also allow for the quick formation of planetesimals through the streaming instability. The streaming instability is most efficient when the grain(s) Stokes number is close to 0.1 (e.g., Carrera et al. 2015). This corresponds to 3–10 cm for IM Lup at 10 au assuming the surface density from Zhang et al. (2021). This is on the large end of the size distribution consistent with the dust continuum modeling (1 cm, assuming $p = -2.5$; Sierra et al. 2021) but also agrees with large grain models that are weakly scattering (Zhu et al. 2019). Grains down to Stokes numbers of 3×10^{-4} (~ 0.1 mm) have also been found to be able to trigger the streaming instability at a gas-to-dust ratio of 10, as measured for IM Lup. Even if grains are small in the inner disk, triggering the streaming instability remains likely. Planetesimals could thus be currently forming through the streaming instability in the inner 20 au of IM Lup.

Strong pebble drift can have a profound impact on the composition of the gas in the inner disk (e.g., Ciesla & Cuzzi 2006; Booth & Ilee 2019), with the pebbles bringing in oxygen-rich ices that lower the C/O ratio within the CO_2 and H_2O ice lines. It has been proposed that these effects can be seen in mid-infrared spectra of these sources, by enhancement of the oxygen-carrying species, H_2O and CO_2 , and subsequent suppression of the carbon-rich species (Najita et al. 2013; Bosman et al. 2018; Banzatti et al. 2020).

The Spitzer-IRS IM Lup spectrum shows a clear CO_2 emission feature at 15 μm but does not show any H_2O , OH, C_2H_2 , or HCN emission, making it a peculiar source in the T Tauri sample (Pontoppidan et al. 2010; Salyk et al. 2011; Bosman et al. 2017). It is not consistent with disks with strong water emission and weak HCN emission, as expected for a disk with strong drift (Najita et al. 2013; Banzatti et al. 2020). However, in the case of strong drift and vertical mixing, Bosman et al. (2018) found extremely elevated CO_2 abundances, resulting in CO_2 -branch fluxes far brighter than observed toward any disk.

The low gas-to-dust ratio inferred for the inner disk of IM Lup might solve this disparity. The strong-line emission observed in many other T Tauri disks in the mid-infrared, which is originating from the surface layers of the inner few au, generally requires high (>1000) gas-to-dust ratios to reproduce (Meijerink et al. 2009; Blevins et al. 2016; Bosman et al. 2017). This is in sharp contrast to the gas-to-dust ratios of 0.1–10 derived from the ALMA data. If these low gas-to-dust ratios persist into the inner-disk upper atmosphere, they would lower the CO_2 flux. This would also smother the C_2H_2 and HCN flux and could make the H_2O lines too weak to detect, leaving only the strong CO_2 Q-branch. Sensitive JWST-MIRI spectra will be able to look for the weak H_2O lines to constrain the CO_2 -to- H_2O abundance ratio. These observations can potentially also detect H_2 pure rotational lines to determine the absolute CO_2 abundance and gas-to-dust ratio in the surface layers.

6.2. Tracing the Gas Cavity in GM Aur

In the millimeter continuum images the GM Aur disk stands out in the MAPS sample, as it has a large cavity in the

dust, with very little large dust within ~ 40 au (e.g., Dutrey et al. 2008; Huang et al. 2020; Sierra et al. 2021). This implies that there is not enough dust to affect the CO line emission. The surface brightness profiles show that the lines still emit from part of the dust cavity, but that there is a strong drop in surface brightness, at least a factor of 3, in all isotopologues. This is significantly larger than the $\sim 30\%$ drop seen in the radial profiles extracted from the images (see Figure 13).

Such strong emission drops can only be from column density drops strong enough to make the ^{12}CO and ^{13}CO lines optically thin. Assuming a ^{12}CO -to- ^{13}CO ratio of 69 (Wilson & Rood 1994), this means that the CO column must drop by almost 2 orders of magnitude between 20 au, where the drop in ^{13}CO begins, and 15 au, where the drop in ^{12}CO begins. As CO strongly self-shields, it is likely that this is due to a total column density drop, with the H_2 column dropping below $\sim 10^{21} \text{ cm}^{-2}$ around 15 au (Bruderer et al. 2012; Bosman et al. 2019), but source-specific models, including isotope-specific photodissociation, are necessary to extract a more detailed CO and H_2 column density profile.

6.3. Impact of Gaps and Rings

The C^{18}O surface brightness profiles in the inner disks of both HD 163296 and AS 209 show gaps and peaks that line up with known dust substructures for these disks imaged at ~ 40 mas (see Figure 5; Andrews et al. 2018; Huang et al. 2018). The bright continuum rings, which exist at 14 au for both disks, line up with a strong ($>3\times$) decrease in the C^{18}O surface brightness. In contrast, at the location of millimeter continuum gaps, at 9 and 10 au for AS 209 and HD 163296, respectively, there is an increase in C^{18}O surface brightness. In AS 209, the 9 au millimeter continuum gap also corresponds to a peak of the ^{12}CO and ^{13}CO surface brightness. This correspondence between continuum rings and line minima implies that the dust is impacting the line emission in these regions. This, in turn, implies either that the dust in these rings has very little scattering opacity at 1.3 mm (grain sizes <0.1 mm or >10 cm) or millimeter dust that is vertically extended (see Section 5.2). In both cases, the ring would need to contain a significantly larger surface density of dust, by at least a factor of 10, when compared to the surrounding material using the surface densities given by Zhang et al. (2021). The presence of a ring signals efficient radial concentration of dust; vertical concentration of dust is also expected. This argues against vertically extended efficiently scattering grains. Furthermore, small grains <0.1 mm would have small Stokes numbers and would thus not be efficiently trapped within the ring. As such, efficient localized growth in the ring to multiple centimeter-sized grains seems to be the most logical explanation.

The increase in C^{18}O flux at the millimeter continuum gaps in AS 209 and HD 163296 is consistent with optically thin dust at these radii, with higher fluxes caused by the lower continuum flux. Reduced continuum opacity allows for a higher column of CO to be probed. At the same time, it implies that the dust gap is rich in gas, as a strongly gas-depleted region at the location of the millimeter continuum gap would cause weak C^{18}O emission from the gap. The peak of ^{12}CO and ^{13}CO in AS 209 around the 9 au millimeter continuum gap suggests that the gap does impact the temperature structure, with higher temperatures in and around this gap. AS 209 also shows a strong drop in

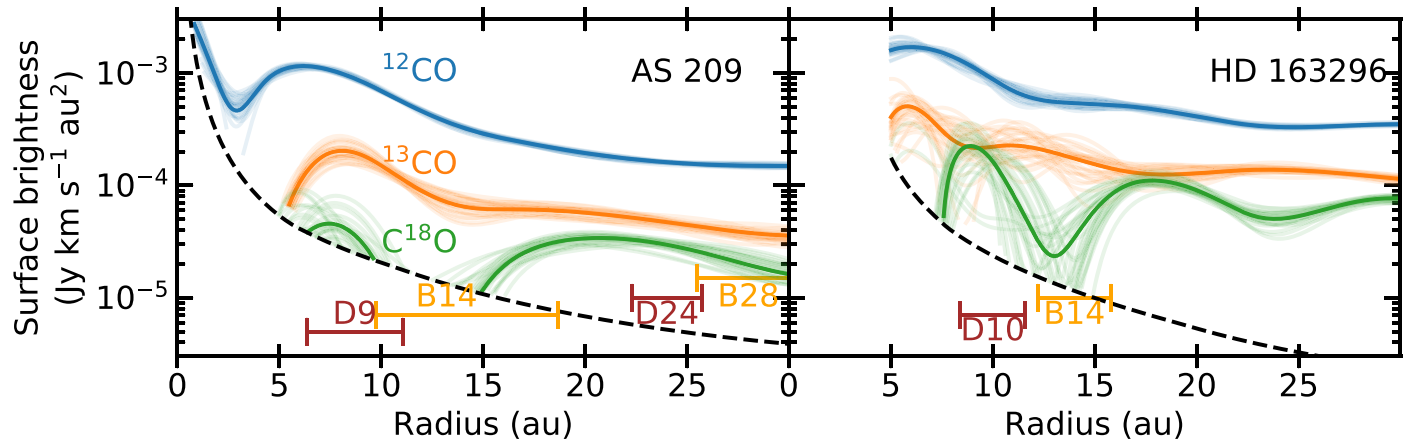


Figure 5. Line-profile-derived radial structures for AS 209 and HD 163296, together with dust substructures found in the DSHARP ALMA large program (Andrews et al. 2018; Huang et al. 2018). Locations and width of bright rings are given in orange, dark gaps in brown. Line colors and styles for the radial profiles are the same as in Figure 2. In both AS 209 and HD 163296 C¹⁸O line emission peaks at the location of the dust gap, while line emission is suppressed at the location of the dust ring.

¹²CO surface density at ~ 3 au, where the ¹³CO has already dropped under the detection threshold. The drop from the peak at 8 au is greater than a factor of 2, implying either a similar drop in temperature or a drop of the CO column density below $\sim 10^{17}$ cm⁻², making CO optically thin. Interestingly, for the second continuum gap-ring pair at 24 and 28 au a clear effect on the C¹⁸O is missing.

6.4. Unresolved Dust Structure in MWC 480?

The MWC 480 disk shows a drop in C¹⁸O surface brightness and a peak in ¹³CO surface brightness at 10 au. High-resolution continuum observations do not show any structure in the inner regions of the MWC 480 disk (Long et al. 2018; Sierra et al. 2021). However, the highest resolution available is 0.08 mas, or 13 au, which would smear out any structure around 10 au.

The combination of a C¹⁸O drop and a ¹³CO peak is difficult to explain. The increase in ¹³CO, and to a lesser extent ¹²CO, implies an increase in gas temperature. The drop in C¹⁸O would imply an optically thin C¹⁸O column, while ¹³CO is still optically thick. This would constrain the CO column density between 3×10^{18} cm⁻² and 2×10^{19} cm⁻² (assuming 50 K for the kinetic temperature). This is at least 3–4 orders of magnitude lower compared to the CO column derived by reproducing the CO isotopologue emission with a thermochemical model and the column necessary to explain the hyperfine line ratios of the C¹⁷O $J = 1-0$ emission originating from the inner regions of the MWC 480 disk (Zhang et al. 2021). As such, it might be more likely that we are tracing some more complex interplay between unresolved dust substructure and temperature.

6.5. Future Directions

Analysis of the dust in the inner regions of IM Lup, HD 163296, and MWC 480 in Sierra et al. (2021) suggests that the grains responsible for the millimeter emission might be small (0.1 mm). These small grains have little scattering opacity at 1.3 and 3 mm and thus efficiently block the line emission (see Section 5.2). At higher frequency, the scattering opacity of these small grains increases relative to the absorption opacity. This would, counterintuitively, increase the expected line flux of high-frequency lines and would allow the use of ¹³CO and C¹⁸O $J = 8-7$ lines to constrain the grain size in the inner disk. At high frequency (877 GHz; ALMA, Band 10) integrations

would be shorter, compared to observations with a similar sensitivity at lower frequency (110 GHz; ALMA Band 3).

Emission originating from the inner disk needs to be bright to allow for the extraction high-resolution surface brightness radial profiles of the inner ~ 20 au from the spectra. This unfortunately constrains the available species that can be used. CO isotopologues, as used here, are the prime candidates. In disks with abundant dust in the inner tens of astronomical units, HCN is the only other species bright enough to extract high-resolution radial surface brightness profiles, but it has the issue of satellite lines that complicate the analysis. In GM Aur, more species are centrally peaked, including CN, CS, and C₂H. This allows for a high-resolution chemical study of the GM Aur disk cavity, and possibly other transition disks, without going to $\ll 0''.15$ resolution. For lines that are weak in the inner disk it is still possible to get upper limits to the surface brightness profile, which can still provide valuable information (see Bosman et al. 2021).

Finally, using a space- or Moon-based submillimeter telescope with a high resolving power instrument ($R = \lambda/\delta\lambda > 10^6$), such as the Origins Space Telescope equipped with HERO (Heterodyne Receiver for Origins), it would be possible to use this technique on bright H₂O water lines, mapping water to far within the telescope’s nominal spatial resolution.

7. Conclusions

We have studied the inner 20 au, using wings of the CO isotopologue lines observed with the MAPS program (Oberg et al. 2021). Using Keplerian rotation of the disk we have inferred radial surface brightness profiles with an effective resolution of ~ 3 au. Our conclusions from these radial surface brightness profiles are as follows:

1. The $J = 1-0$ and $J = 2-1$ ¹³CO and C¹⁸O line wings are consistent within the observational errors for all sources. This implies that the lower-frequency $J = 1-0$ lines do not probe significantly deeper down toward the midplane than the $J = 2-1$ lines.
2. Radial surface brightness profiles extracted from the line profiles show a host of features, including gaps and peaks in the C¹⁸O surface brightness in AS 209, HD 163296, and MWC 480; an inner hole in ¹³CO and C¹⁸O in IM Lup (20–30 au) and AS 209 (5 au); and an inner hole in

- ^{12}CO , ^{13}CO , and C^{18}O in GM Aur. Some of these features are not resolved in the CLEANED images, showcasing the power of this technique.
3. The central depletion of CO isotopologue emission seen for GM Aur is consistent with a gas cavity within the dust cavity as previously inferred (e.g., Dutrey et al. 2008). We estimate that ^{12}CO is optically thin within 15 au.
 4. The inner hole in the CO emission in IM Lup can be explained by a pileup of large dust in the inner 20 au. This is in line with multiwavelength continuum emission analysis and implies that there is $>400 M_{\oplus}$ of large dust and a gas-to-dust ratio of $\lesssim 10$ within 20 au in the IM Lup disk. We propose that this pileup is due to radial drift of large dust. The drift rate necessary to cause this pileup, $>100 M_{\oplus} \text{ Myr}^{-1}$, enables the quick formation of giant planet cores through pebble accretion, while the small gas-to-dust ratios would allow for the triggering of the streaming instability.
 5. The previously resolved continuum rings in the inner 20 au of AS 209 and HD 163296 appear to impact the CO isotopologue emission. The innermost bright continuum ring in both systems is cospatial with a drop in the C^{18}O surface brightness, while the millimeter continuum gap inward of this shows an emission peak in all isotopologues in both disks. Efficient growth of grains to multiple-centimeter sizes within the continuum ring, coupled with trapping of these grains, can explain the lack of CO emission.
 6. The CO isotopologue surface brightness in the inner disk of MWC 480 shows a strong variation in the ^{13}CO and C^{18}O surface brightness at 10 au, for which no explanation has been found.

This paper makes use of the following ALMA data: ADS/JAO.ALMA#2018.1.01055.L. ALMA is a partnership of ESO (representing its member states), NSF (USA) and NINS (Japan), together with NRC (Canada), MOST and ASIAA (Taiwan), and KASI (Republic of Korea), in cooperation with the Republic of Chile. The Joint ALMA Observatory is operated by ESO, AUI/NRAO and NAOJ. The National Radio Astronomy Observatory is a facility of the National Science Foundation operated under cooperative agreement by Associated Universities, Inc.

A.D.B., E.A.B., K.I.Ö., and F.A. acknowledge support from NSF AAG grant No. 1907653. S.M.A. and J.H. acknowledge funding support from the National Aeronautics and Space Administration under grant No. 17-XRP17 2-0012 issued through the Exoplanets Research Program. M.L.R.H. acknowledges support from the Michigan Society of Fellows. R.T. and F.L. acknowledge support from the Smithsonian Institution as a Submillimeter Array (SMA) Fellow. K.I.Ö. acknowledges support from the Simons Foundation (SCOL No. 321183). V.V.G. acknowledges support

from FONDECYT Iniciación 11180904 and ANID project Basal AFB-170002. C.W. acknowledges financial support from the University of Leeds and from the Science and Technology Facilities Council (grant Nos. ST/R000549/1 and ST/T000287/1). Y.A. acknowledges support by NAOJ ALMA Scientific Research grant code 2019-13B and Grant-in-Aid for Scientific Research Nos. 18H05222 and 20H05847. J.B., J.B.B., I.C., J.H., K. R.S., and K.Z. acknowledge support by NASA through the NASA Hubble Fellowship grant Nos. HST-HF2-51427.001-A, HST-HF2-51429.001-A, HST-HF2-51405.001-A, HST-HF2-51460.001-A, HST-HF2-51419.001, and HST-HF2-51401.001, awarded by the Space Telescope Science Institute, which is operated by the Association of Universities for Research in Astronomy, Incorporated, under NASA contract NAS5-26555. G.C. is supported by NAOJ ALMA Scientific Research grant code 2019-13B. L.I.C. gratefully acknowledges support from the David and Lucile Packard Foundation and Johnson & Johnson’s WiSTEM2D Program. A.S.B. acknowledges the studentship funded by the Science and Technology Facilities Council of the United Kingdom (STFC). J.D.I. acknowledges support from the Science and Technology Facilities Council of the United Kingdom (STFC) under ST/T000287/1. C.J.L. acknowledges funding from the National Science Foundation Graduate Research Fellowship under grant No. DGE1745303. R.L.G. acknowledges support from a CNES fellowship grant. Y.L. acknowledges the financial support by the Natural Science Foundation of China (grant No. 11973090). F.M. acknowledges support from ANR of France under contract ANR-16-CE31-0013 (Planet-Forming-Disks) and ANR-15-IDEX-02 (through CDP “Origins of Life”). H.N. acknowledges support by NAOJ ALMA Scientific Research grant code 2018-10B and Grant-in-Aid for Scientific Research 18H05441. L.M.P. acknowledges support from ANID project Basal AFB-170002 and from ANID FONDECYT Iniciación project No. 11181068. A.S. acknowledges support from ANID/CONICYT Programa de Astronomía Fondo ALMA-CONICYT 2018 31180052. T.T. is supported by JSPS KAKENHI grant Nos. JP17K14244 and JP20K04017. Y.Y. is supported by IGPEES, WINGS Program, the University of Tokyo. K.Z. acknowledges the support of the Office of the Vice Chancellor for Research and Graduate Education at the University of Wisconsin–Madison with funding from the Wisconsin Alumni Research Foundation.

Appendix A Line Profiles

A.1. Asymmetries in the CO J = 2–1 Line Profiles

To extract the radial profiles, we assume that all emission originates from a flat Keplerian disk. While it is impossible to ascertain whether emission is actually coming from a Keplerian disk without resolving the emission, it is possible to look for non-Keplerian gas by looking at the asymmetries in the line emission. Wherever this symmetry is broken, line emission on

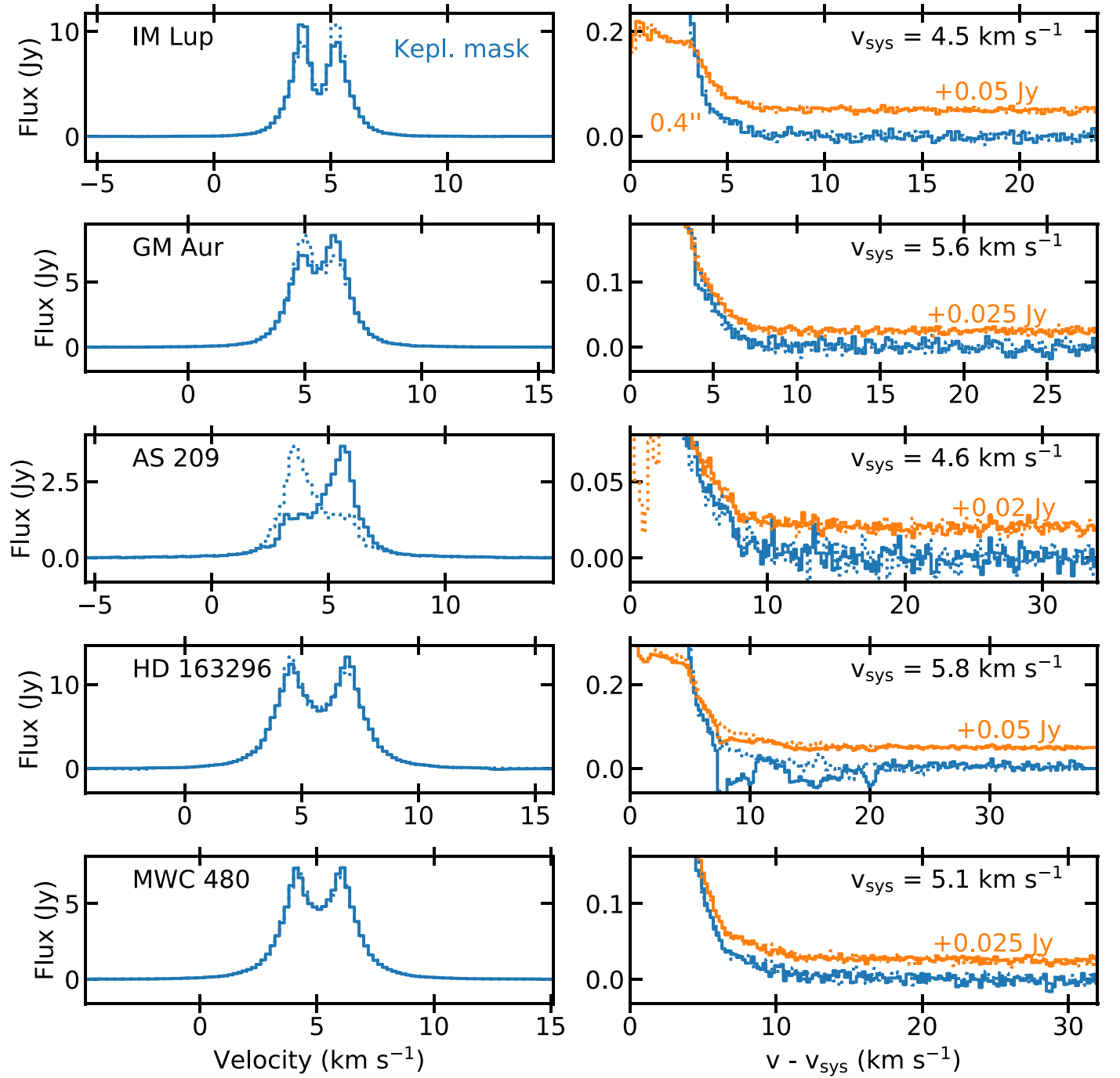


Figure 6. $^{12}\text{CO } J=2-1$ spectra for the five MAPS sources. Spectra in blue are extracted by integrating over the cleaning mask in each channel. Each spectrum has been mirrored around the source velocity; this is plotted in dotted lines. The right column shows a zoom-in of these spectra, plotted against the offset from source velocity. The red side is shown with solid lines, while the dashed lines show the blue side. In orange a spectrum extracted with a smaller circular aperture is shown; these are offset in flux for clarity. In the left column, some clear asymmetries in the line profiles at small velocity offsets can be seen, due to either large-scale disk structures (GM Aur, IM Lup, and HD 163296) or foreground emission (AS 209). The spectra for GM Aur, IM Lup, and MWC 480 at high velocities, and hence small radii, are very symmetric. HD 163296 shows significant asymmetry at large velocity offsets, and AS 209 shows an anomalously high flux on the red side at 5.9 km s^{-1} offset (10.5 km s^{-1} in local standard of rest). These features are shown in more detail in Figure 7.

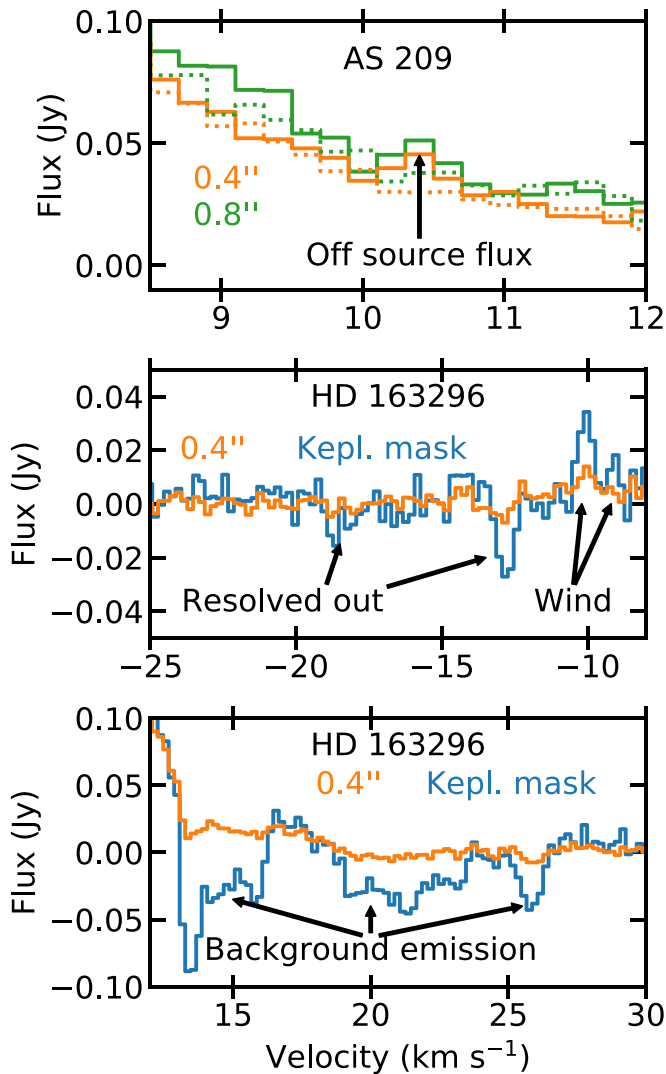


Figure 7. Zoom-in of the $^{12}\text{CO } J=2-1$ spectra for the asymmetric features in AS 209 and HD 163296. Spectra in blue (HD 163296 only) are extracted by integrating over the cleaning mask in each channel, the orange spectra from a circular aperture of $0''.4$, and the green spectra (AS 209 only) from a circular aperture of $0''.8$. The AS 209 spectrum also shows the mirror spectrum in green. All features have been labeled. The flux spike in AS 209 (top), most clearly seen in the $0''.8$ spectrum, is assumed to be due to a noise spike. The excess emission on the blue side of HD 163296 (middle) is due to wind emission falling within the Keplerian mask, whereas the negative fluxes are due to the fringing caused by the strong and extended wind emission. On the red side of HD 163296 (bottom), strong negative fluxes are measured in the Keplerian mask, as the disk is backlit by galactic CO emission at these velocities, creating negatives in the continuum-subtracted images where there is dust emission.

either the blue- or redshifted side of the line is certainly not coming from a Keplerian disk. These asymmetries should be most obvious in the ^{12}CO spectra.

Figure 6 shows the $^{12}\text{CO } J=2-1$ spectra and their mirror image, in velocity space, for the five MAPS disks. The systematic velocities as tabulated in Table 1 are used to mirror the line profiles. At velocities close to the systemic velocity in Figure 6, differences between the low-velocity red- and blueshifted emission can be seen for AS 209, IM Lup, GM Aur, and HD 163296. These line asymmetries can all be ascribed to factors discussed elsewhere (foreground absorption, nondisk emission, disk flaring; Huang et al. 2021; Law et al. 2021). The line wings for IM Lup, GM Aur, and MWC 480 show very symmetric

emission, suggesting that a Keplerian disk is a good approximation. AS 209 and HD 163296 show features that warrant further investigation. Regions of interest are plotted in Figure 7.

AS 209 shows a feature around 10.5 km s^{-1} . There is a two-channel, 6σ – 7σ flux spike that is offset from the source and is thus stronger in the $0''.8$ aperture than the $0''.4$ aperture (see Figure 7). The image cubes show a compact emission component $\sim 0''.3$ offset from the disk center. This component does not have a counterpart in $^{13}\text{CO } J=2-1$, nor in the DSHARP $J=2-1$ ^{12}CO data cubes (Andrews et al. 2018). The feature is considered anomalous, and the channels around this region are masked in the rest of the analysis.

The spectrum of HD 163296 is very messy at high velocity offsets. On the blue side of source velocity there is a known CO outflow (Klaassen et al. 2013; Booth et al. 2021). Around -10 km s^{-1} some of the emission from the outflow is contaminating our on-source spectra, especially in the Keplerian CLEANing mask.²⁷ Between -12 and -20 km s^{-1} there are some negative flux features in the spectrum. The velocities of these correspond to velocities at which the outflow is bright and extended. As the full extent of the outflow is not properly captured in the interferometric data, this induces a fringe pattern over the entire reconstructed image, leading to negative fluxes at some velocities. As both the flux contribution due to the outflow and the modification to the flux due to fringing are hard to quantify, all channels with velocities between -25 and -9 km s^{-1} are excluded from further analysis.

On the red side of the spectrum of HD 163296, strong negative fluxes can be seen in the spectrum extracted within the Keplerian CLEANing mask between 13 and 26 km s^{-1} . The image cubes show evidence of strong CO emission behind the disk at these velocities. This backlighting of the disk leads to the dust disk showing up as a negative in these continuum-subtracted images, and the large-scale nature of the background emission leads to strong fringing, further modifying the flux. Again we have decided to remove these velocities from further analysis. As both the red and blue sides of the spectrum are unusable at high velocities, our radial profile extraction is limited to radii larger than 5 au in HD 163296. Future observations, with better short baseline spacing, should be able to resolve some of these problems, allowing us to extract an accurate inner disk CO flux from these high-velocity channels.

A.2. $^{13}\text{CO } J=2-1$ and $J=1-0$ Comparison

In the absence of a dust cavity, dust in the inner regions of protoplanetary disks is so abundant that it should be optically thick at millimeter wavelengths. It is generally assumed that, due to the lower opacity at longer wavelength, observations at longer wavelength can penetrate significantly deeper into the disk, leading to brighter (in units of K) lines. The difference in dust extinction opacity between 0.3 and 3 mm (approximately the wavelength range currently covered by ALMA) is assumed to be less than an order of magnitude in a standard large grain (sizes up to 1 mm) dust model (e.g., Birnstiel et al. 2018). This suggests that the differences in probed column and line fluxes might be small. The MAPS data cover both the $J=2-1$ (220 GHz) and the $J=1-0$ (110 GHz) ^{13}CO lines at high resolution ($<0''.3$) and sensitivity. Higher probing depth, due to the lower dust opacity, of the lower-frequency line should show

²⁷ The CLEANing mask at these velocities is large enough to capture the size of the dust disk and is thus about $3''$ across.

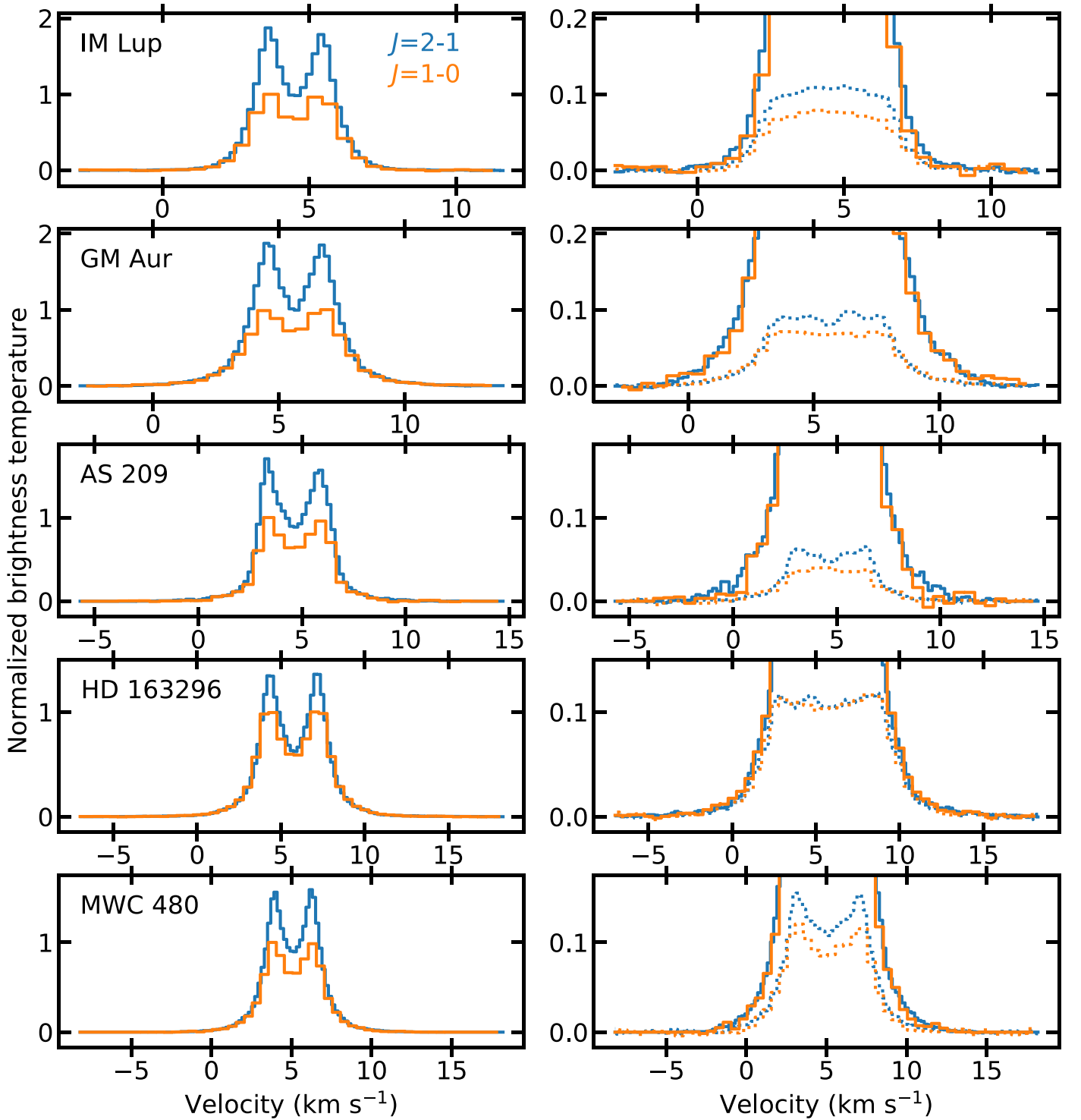


Figure 8. Comparison of the $^{13}\text{CO } J=2-1$ (blue) and $^{13}\text{CO } J=1-0$ (orange) line profiles. The profiles are normalized to the $J=1-0$ line. The left panel shows the full line profile, while the right panel shows a more constrained brightness temperature range, with spectra extracted with a $1''$ aperture as dotted lines. The profiles are scaled to a brightness temperature scale assuming the Rayleigh–Jeans law, which underestimates the $J=2-1$ line strength (see Section A.2). For velocities close to the systemic value, the $J=2-1$ line is consistently brighter than the $J=1-0$ line, indicating either that the ^{13}CO flux is optically thin or that the $J=2-1$ flux comes from a warmer layer than the $J=1-0$. In the line wings, however, it seems that both lines are equally bright. This indicates that both the $J=2-1$ and the $J=1-0$ lines are optically thick.

in source spectra as excess line wing flux, when compared on equal scales. The Band 3 (3 mm, $J=1-0$) and Band 6 (1.3 mm, $J=2.1$) line profiles of ^{13}CO and C^{18}O are compared in Figures 8 and 9, respectively. The $J=2-1$ lines are scaled down by a factor of 4 to compensate for the Rayleigh–Jeans relation, $I \propto \nu^2 T$. Compared to the full Planck law, this

underestimates the $J=2-1$ flux by 10% at 30 K, and with values agreeing better at higher temperatures.

Figures 8 and 9 show that, near the systemic velocity, the $J=2-1$ line is consistently brighter than the $J=1-0$ line. This can be understood from the Einstein A -coefficients and molecular level structure, which predicts an optical depth ratio

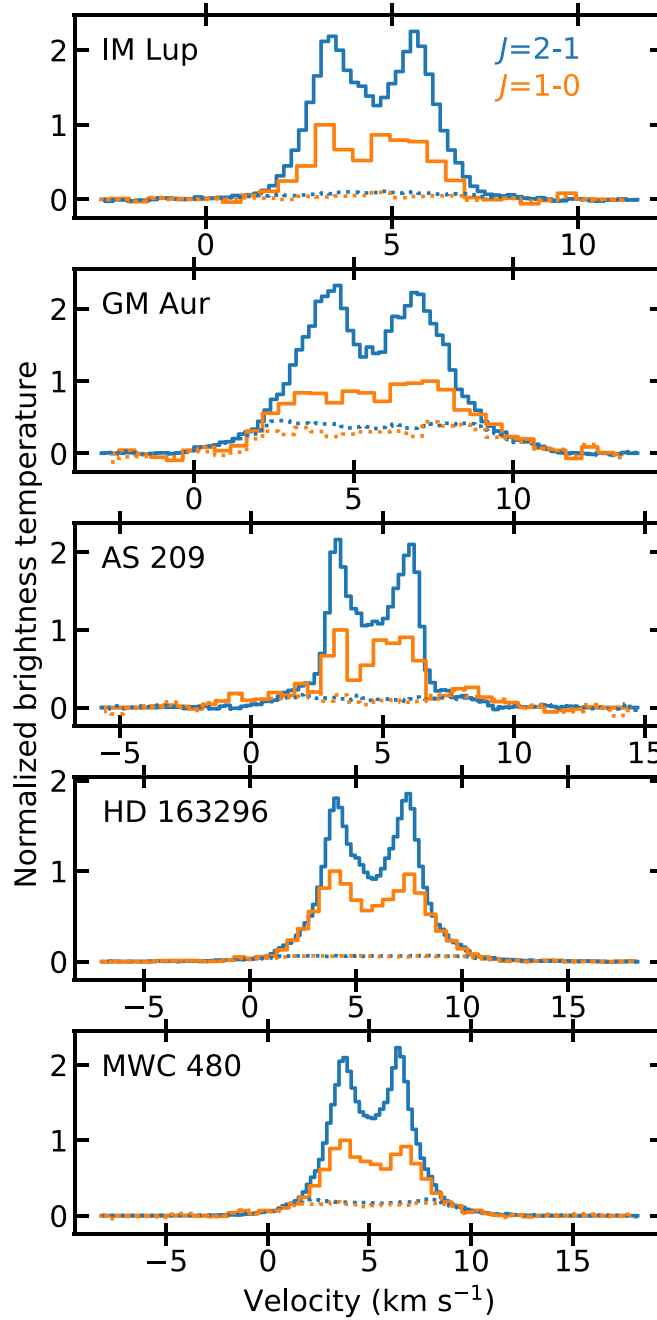


Figure 9. Comparison of the $\text{C}^{18}\text{O } J=2-1$ (blue) and $\text{C}^{18}\text{O } J=1-0$ (orange) line profiles; solid lines show the profiles extracted with the Keplerian cleaning mask, and the spectrum extracted with a $0.4''$ aperture is shown with dotted lines. The profiles are scaled to a brightness temperature scale assuming the Rayleigh–Jeans law, which underestimates the $J=2-1$ line strength (see Section A.2). Similar to Figure 8, no evidence of stronger emission in Band 3 is seen compared to Band 6 in the line wings.

(and thus brightness temperature ratio if both lines are optically thin) between the $J=2-1$ and $J=1-0$ lines of 2.7–3 for gas of 20–30 K (Schöier et al. 2005; Endres et al. 2016). These ratios are not reached, implying a strong contribution from optically thick $J=2-1$ line flux even at low velocities relative to the source. In the line wings, however, the $J=2-1$ and $J=1-0$ spectra have indistinguishable emission temperatures, as expected for optically thick lines with the same T_{ex} . In the inner ~ 40 au the $J=1-0$ and $J=2-1$ line thus originate for a

very similar layer. This indicates that the lower dust opacity at Band 3 is not allowing the observations to probe deeper into the disk compared to higher-frequency bands.

Appendix B Surface Brightness Fitting Process

The fitting process to extract radial surface brightness profiles from the line profile wings is given schematically in Figure 10. The fitting procedure starts with creating the

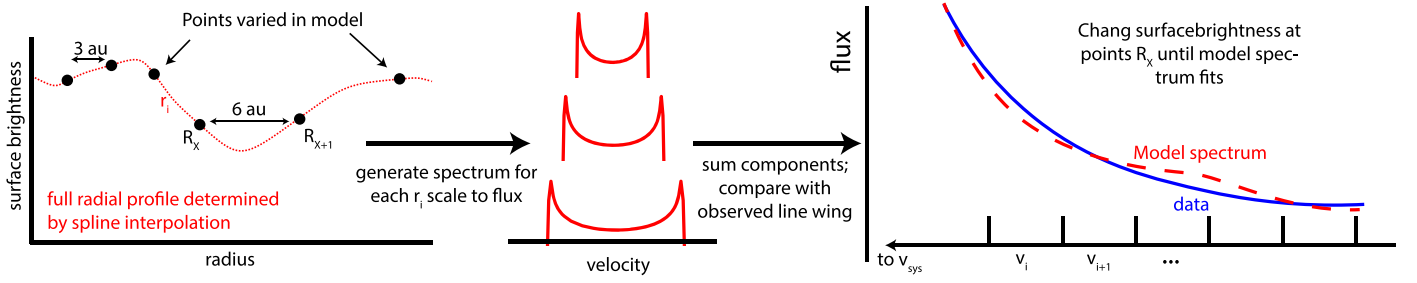


Figure 10. Schematic representation of the fitting process. The left panel shows the input points, R_X , in black. These points have semiregular spacing of 3, 6, and 12 au (see Figure 12) for the radial locations of these points. From the surface brightness at points R_X , the surface brightness at a secondary grid, r_i , is calculated by spline interpolation. The points r_i are spaced in radius such that their $v_{\max}(r_i)$ are regularly spaced in velocity with a 0.025 km s^{-1} spacing. For each of these radii r_i the spectrum of an annulus of this radius is calculated and scaled to the required intensity (middle). These spectral components are summed to calculate the full line profile. This is then compared to the observed line profile (right). The intensity at the points R_X is then varied until there is a match between observed and modeled spectrum.

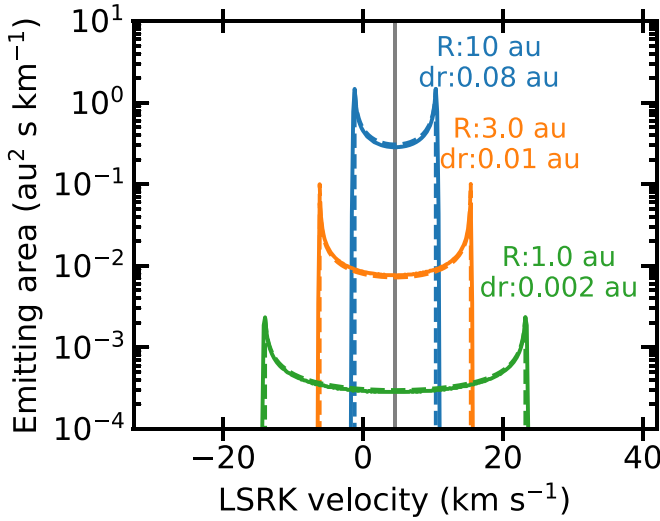


Figure 11. Shape and strength of three components used in the fitting procedure of the AS 209 disk (solid lines) compared to the analytic shape (Equation (B1); dashed lines). The components have been convolved with a Gaussian of 0.2 km s^{-1} , which accounts for the slight differences from the analytic shape. For each component both the radius and the width of the annulus it represents are given.

forward-model components that have a Keplerian line shape, corresponding to an annulus in the disk at a given radius. The shape is given by

$$f(v) = \frac{1}{\sqrt{v_{\max}^2 - v^2}}, \quad (\text{B1})$$

with v_{\max} as in Equation (1). These components are convolved with a 0.2 km s^{-1} FWHM Gaussian to account for instrumental and physical broadening of the line and then normalized to their surface area, which is influenced by the spacing between flux components; examples of components for the AS 209 disk are shown in Figure 11.

To correctly fit the line profile wings, the underlying emission model needs to have enough resolution to fully represent the disk emission. Given that the spectra are not Nyquist sampled and that the sampling is smaller than the expected line width,²⁸ the velocity spacing of the components has to be smaller than the bin size. Here we use a spacing that is

²⁸ Only for $T > 100 \text{ K}$ is the thermal line width larger than the 0.2 km s^{-1} velocity resolution.

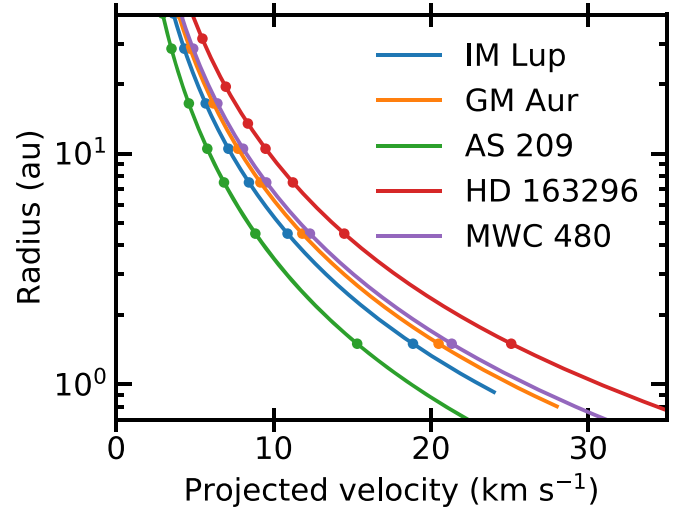


Figure 12. Relation between projected velocity offset and Keplerian radius (Equation (1)), as well as the radial grid points used in the fitting procedure, assuming a minimum of three velocity bins per radial bin.

8 times smaller, leading to model components (r_i in Figure 10) being spaced by 0.025 km s^{-1} , and irregularly spaced in radius. This leads to 500–2000 components for a single line. This is far too many to fit individually. Therefore, a lower-resolution grid is made (R_X in Figure 10), the intensities at these radii are varied as the free parameters to the fitting problem, and the intensity of the model components that actually make up the final spectrum is derived from these by spline interpolation.

To leverage the sensitivity of this technique at small radii, this grid is irregular in radius space as well. The fitting points are initially spaced by 3 au; when the projected Keplerian velocity difference between two points becomes less than 0.6 km s^{-1} , the grid spacing is increased to 6 au; and when this is still not enough, it is increased to 12 au. As such, our radial surface brightness profiles have a lower resolution at larger radii. The radii at which these points fall are shown in Figure 12.

Appendix C Comparison with Image Radial Profiles

Figure 13 shows the line-profile-extracted surface brightness profiles with the image-derived profiles. The profiles agree on the absolute level of flux, but the line-profile-extracted profiles show more and sharper features.

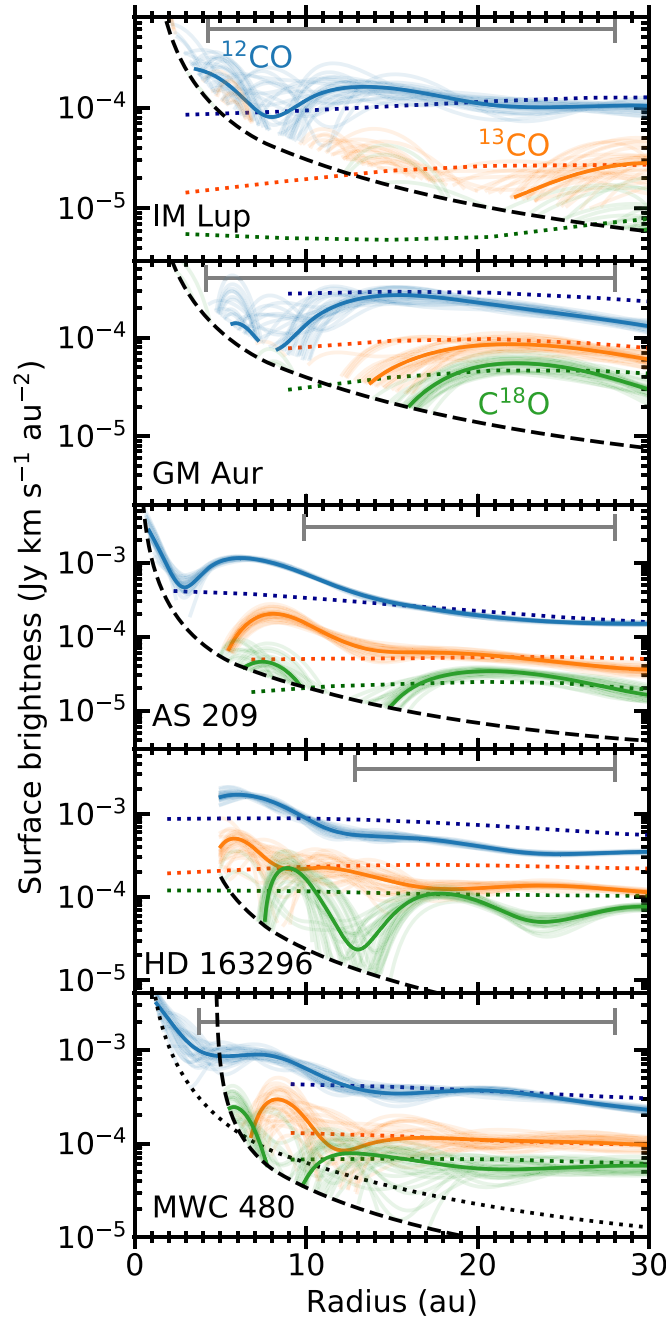


Figure 13. Same as Figure 2, but with the image-cube-extracted radial profiles (dotted; Law et al. 2021). Gray bars show the nominal MAPS resolution of $0.15''$. Image radial profile extraction is done on the fiducial $0.15''$ resolution MAPS images with a 15° wedge for all lines except the ^{12}CO line in AS 209, where a one-sided 55° wedge is used (see Law et al. 2021; no vertical emission height has been assumed for any of these radial profiles).

Appendix D Toy Model Setup

To test the effect of large dust in a realistic setting, a couple of models using Dust and Lines (DALI; Bruderer et al. 2012; Bruderer 2013) have been used. A simple T Tauri disk motivated by the results from Zhang et al. (2021) for IM Lup is used for this purpose. Model parameters can be found in Table 2. Most critically, the gas surface density is chosen such that the CO column in the inner disk is approximately 10^{19} cm^{-2} around 40 au and has a CO abundance of 10^{-5} , 1 order of

magnitude reduced from interstellar medium levels. The disk gas-to-dust ratio is taken to be 100, with 99% of this dust as large dust settles to the midplane, creating a disk that is only optically thick around 200 GHz within 5 au.

The models vary in the treatment of the large dust within 20 au. For the fiducial model the large dust within 20 au is settled at 20% of the gas scale height and the vertically integrated gas-to-dust ratio is 100. The three other models have the dust vertically well mixed with the gas within 20 au. This causes the gas- and dust-emitting regions to overlap. Furthermore, the vertically integrated gas-to-dust ratio is varied

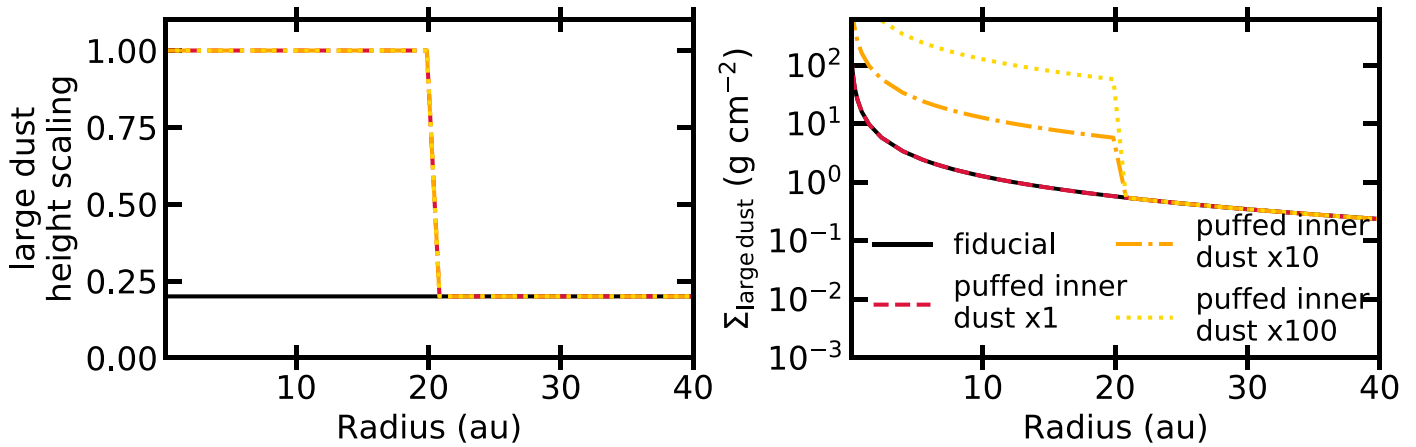


Figure 14. Large dust scale height with respect to the gas scale height (left) and large dust surface density (right) in the DALI models.

Table 2
Toy Model Parameters

Parameter	Value
M_*	$1 M_\odot$
Stellar spectrum	IM Lup ^a
L_X	$4 \times 10^{30} \text{ erg s}^{-1}$
$\Sigma_{c, \text{gas}}$	28.4 g cm^{-2}
R_c	100 au
h_c	0.1
γ	1
ψ	0.17
C/H	1.35×10^{-5}
O/H	2.88×10^{-5}
N/H	2.1×10^{-6}

Note.

^a Zhang et al. (2021).

between 1 and 100, by increasing the amount of dust by up to a factor of 10. Large dust surface densities and scale height distribution are shown in Figure 14.

ORCID iDs

Arthur D. Bosman <https://orcid.org/0000-0003-4001-3589>
 Edwin A. Bergin <https://orcid.org/0000-0003-4179-6394>
 Ryan A. Loomis <https://orcid.org/0000-0002-8932-1219>
 Sean M. Andrews <https://orcid.org/0000-0003-2253-2270>
 Merel L. R. van 't Hoff <https://orcid.org/0000-0002-2555-9869>
 Richard Teague <https://orcid.org/0000-0003-1534-5186>
 Karin I. Öberg <https://orcid.org/0000-0001-8798-1347>
 Viviana V. Guzmán <https://orcid.org/0000-0003-4784-3040>
 Catherine Walsh <https://orcid.org/0000-0001-6078-786X>
 Yuri Aikawa <https://orcid.org/0000-0003-3283-6884>
 Felipe Alarcón <https://orcid.org/0000-0002-2692-7862>
 Jaehan Bae <https://orcid.org/0000-0001-7258-770X>
 Jennifer B. Bergner <https://orcid.org/0000-0002-8716-0482>
 Alice S. Booth <https://orcid.org/0000-0003-2014-2121>
 Gianni Cataldi <https://orcid.org/0000-0002-2700-9676>
 L. Ilse-dore Cleaves <https://orcid.org/0000-0003-2076-8001>
 Ian Czekala <https://orcid.org/0000-0002-1483-8811>
 Jane Huang <https://orcid.org/0000-0001-6947-6072>
 John D. Ilee <https://orcid.org/0000-0003-1008-1142>
 Charles J. Law <https://orcid.org/0000-0003-1413-1776>

Romane Le Gal <https://orcid.org/0000-0003-1837-3772>
 Yao Liu <https://orcid.org/0000-0002-7616-666X>
 Feng Long <https://orcid.org/0000-0002-7607-719X>
 François Ménard <https://orcid.org/0000-0002-1637-7393>
 Hideko Nomura <https://orcid.org/0000-0002-7058-7682>
 Laura M. Pérez <https://orcid.org/0000-0002-1199-9564>
 Chunhua Qi <https://orcid.org/0000-0001-8642-1786>
 Kamber R. Schwarz <https://orcid.org/0000-0002-6429-9457>
 Anibal Sierra <https://orcid.org/0000-0002-5991-8073>
 Takashi Tsukagoshi <https://orcid.org/0000-0002-6034-2892>
 Yoshihide Yamato <https://orcid.org/0000-0003-4099-6941>
 David J. Wilner <https://orcid.org/0000-0003-1526-7587>
 Ke Zhang <https://orcid.org/0000-0002-0661-7517>

References

- ALMA Partnership, Brogan, C. L., & Pérez, L. M. 2015, *ApJL*, 808, L3
 Andrews, S. M., Huang, J., Pérez, L. M., et al. 2018, *ApJL*, 869, L41
 Armitage, P. J. 2011, *ARA&A*, 49, 195
 Avenhaus, H., Quanz, S. P., Schmid, H. M., et al. 2017, *AJ*, 154, 33
 Banzatti, A., Pascucci, I., Bosman, A. D., et al. 2020, *ApJ*, 903, 124
 Banzatti, A., & Pontoppidan, K. M. 2015, *ApJ*, 809, 167
 Banzatti, A., Pontoppidan, K. M., Salyk, C., et al. 2017, *ApJ*, 834, 152
 Birnstiel, T., Dullemond, C. P., Zhu, Z., et al. 2018, *ApJL*, 869, L45
 Bitsch, B., Izidoro, A., Johansen, A., et al. 2019, *A&A*, 623, A88
 Blevins, S. M., Pontoppidan, K. M., Banzatti, A., et al. 2016, *ApJ*, 818, 22
 Booth, A. S., Tabone, B., Ilee, J. D., et al. 2021, *ApJS*, 257, 16
 Booth, R. A., & Ilee, J. D. 2019, *MNRAS*, 487, 3998
 Bosman, A. D., Alarcón, F., Bergin, E. A., et al. 2021, *ApJS*, 257, 7
 Bosman, A. D., Banzatti, A., Bruderer, S., et al. 2019, *A&A*, 631, A133
 Bosman, A. D., Bruderer, S., & van Dishoeck, E. F. 2017, *A&A*, 601, A36
 Bosman, A. D., Tielens, A. G. G. M., & van Dishoeck, E. F. 2018, *A&A*, 611, A80
 Brown, J. M., Pontoppidan, K. M., van Dishoeck, E. F., et al. 2013, *ApJ*, 770, 94
 Bruderer, S. 2013, *A&A*, 559, A46
 Bruderer, S., van Dishoeck, E. F., Doty, S. D., & Herczeg, G. J. 2012, *A&A*, 541, A91
 Carmona, A., Thi, W. F., Kamp, I., et al. 2017, *A&A*, 598, A118
 Carr, J. S., & Najita, J. R. 2008, *Sci*, 319, 1504
 Carrera, D., Johansen, A., & Davies, M. B. 2015, *A&A*, 579, A43
 Ciesla, F. J., & Cuzzi, J. N. 2006, *Icar*, 181, 178
 Cleaves, L. I., Bergin, E. A., Öberg, K. I., et al. 2017, *ApJL*, 843, L3
 Cridland, A. J., Pudritz, R. E., & Alessi, M. 2019, *MNRAS*, 484, 345
 Czekala, I., Loomis, R. A., Teague, R., et al. 2021, *ApJS*, 257, 2
 Dubrulle, B., Morfill, G., & Sterzik, M. 1995, *Icar*, 114, 237
 Dullemond, C. P., & Monnier, J. D. 2010, *ARA&A*, 48, 205
 Dutrey, A., Guilloteau, S., Piétu, V., et al. 2008, *A&A*, 490, L15
 Dutrey, A., Guilloteau, S., Piétu, V., et al. 2017, *A&A*, 607, A130

- Endres, C. P., Schlemmer, S., Schilke, P., Stutzki, J., & Müller, H. S. P. 2016, *JMoSp*, **327**, 95
- Ercolano, B., & Pascucci, I. 2017, *RSOS*, **4**, 170114
- Fernandes, R. B., Mulders, G. D., Pascucci, I., Mordasini, C., & Emsenhuber, A. 2019, *ApJ*, **874**, 81
- Gammie, C. F. 1996, *ApJ*, **457**, 355
- Gravity Collaboration, Abuter, R., Accardo, M., et al. 2017, *A&A*, **602**, A94
- Guzmán, V. V., Huang, J., Andrews, S. M., et al. 2018, *ApJL*, **869**, L48
- Hales, A. S., Gorti, U., Carpenter, J. M., Hughes, M., & Flaherty, K. 2019, *ApJ*, **878**, 113
- Huang, J., Andrews, S. M., Dullemond, C. P., et al. 2018, *ApJL*, **869**, L42
- Huang, J., Andrews, S. M., Dullemond, C. P., et al. 2020, *ApJ*, **891**, 48
- Huang, J., Bergin, E. A., Öberg, K. I., et al. 2021, *ApJS*, **257**, 19
- Huang, J., Öberg, K. I., Qi, C., et al. 2017, *ApJ*, **835**, 231
- Johnson, J. A., Aller, K. M., Howard, A. W., & Crepp, J. R. 2010, *PASP*, **122**, 905
- Klaassen, P. D., Juhasz, A., Mathews, G. S., et al. 2013, *A&A*, **555**, A73
- Law, C., Loomis, R. A., Teague, R., et al. 2021, *ApJS*, **257**, 3
- Lazareff, B., Berger, J.-P., Kluska, J., et al. 2017, *A&A*, **599**, A85
- Liu, Y., Dipierro, G., Ragusa, E., et al. 2019, *A&A*, **622**, A75
- Long, F., Pinilla, P., Herczeg, G. J., et al. 2018, *ApJ*, **869**, 17
- Lyra, W., Paardekooper, S.-J., & Mac Low, M.-M. 2010, *ApJL*, **715**, L68
- Macías, E., Espaillat, C. C., Ribas, Á., et al. 2018, *ApJ*, **865**, 37
- Mawet, D., Absil, O., Montagnier, G., et al. 2012, *A&A*, **544**, A131
- Meijerink, R., Pontoppidan, K. M., Blake, G. A., Poelman, D. R., & Dullemond, C. P. 2009, *ApJ*, **704**, 1471
- Menu, J., van Boekel, R., Henning, T., et al. 2015, *A&A*, **581**, A107
- Mulders, G. D. 2018, *Handbook of Exoplanets* (Berlin: Springer), 153
- Najita, J. R., Carr, J. S., Pontoppidan, K. M., et al. 2013, *ApJ*, **766**, 134
- Öberg, K. I., Guzmán, V. V., Walsh, C., et al. 2021, *ApJS*, **257**, 1
- Piétu, V., Dutrey, A., & Guilloteau, S. 2007, *A&A*, **467**, 163
- Pinte, C., Ménard, F., Duchêne, G., et al. 2018, *A&A*, **609**, A47
- Pontoppidan, K. M., Blake, G. A., van Dishoeck, E. F., et al. 2008, *ApJ*, **684**, 1323
- Pontoppidan, K. M., & Blevins, S. M. 2014, *FaDi*, **169**, 49
- Pontoppidan, K. M., Salyk, C., Blake, G. A., et al. 2010, *ApJ*, **720**, 887
- Rosenfeld, K. A., Qi, C., Andrews, S. M., et al. 2012, *ApJ*, **757**, 129
- Rosotti, G. P., Ilee, J. D., Facchini, S., et al. 2021, *MNRAS*, **501**, 3427
- Salyk, C., Pontoppidan, K. M., Blake, G. A., Najita, J. R., & Carr, J. S. 2011, *ApJ*, **731**, 130
- Schöier, F. L., van der Tak, F. F. S., van Dishoeck, E. F., & Black, J. H. 2005, *A&A*, **432**, 369
- Sierra, A., Pérez, L. M., Zhang, K., et al. 2021, *ApJS*, **257**, 14
- Simon, M., Guilloteau, S., Beck, T. L., et al. 2019, *ApJ*, **884**, 42
- Teague, R., Bae, J., & Bergin, E. A. 2019, *Natur*, **574**, 378
- van der Plas, G., van den Ancker, M. E., Waters, L. B. F. M., & Dominik, C. 2015, *A&A*, **574**, A75
- Weaver, E., Isella, A., & Boehler, Y. 2018, *ApJ*, **853**, 113
- Wilson, T. L., & Rood, R. 1994, *ARA&A*, **32**, 191
- Zhang, K., Bergin, E. A., Blake, G. A., Cleaves, L. I., & Schwarz, K. R. 2017, *NatAs*, **1**, 0130
- Zhang, K., Bosman, A. D., & Bergin, E. A. 2020a, *ApJL*, **891**, L16
- Zhang, K., Booth, A. S., Law, C. J., et al. 2021, *ApJS*, **257**, 5
- Zhang, K., Schwarz, K. R., & Bergin, E. A. 2020b, *ApJL*, **891**, L17
- Zhu, Z., Zhang, S., Jiang, Y.-F., et al. 2019, *ApJL*, **877**, L18